Le Béon *et al. Geoscience Letters* (2024) 11:57
https://doi.org/10.1186/s40562-024-00373-3

Geoscience Letters

RESEARCH LETTER **Open Access**

Aseismic deformation within fold-and-thrust belts: example from the Tsengwen River section of southwest Taiwan

Maryline Le Béon[1,2,3*], Chang-Chih Chen[1], Wen-Jeng Huang[1,3], Kuo-En Ching[4], Jhih-Wei Shih[1], Ya-Chu Tseng[1,5], Yi-Wei Chiou[1,6], Yen-Chiu Liu[7], Meng-Long Hsieh[8], Erwan Pathier[9], Chih-Heng Lu[10,11] and Bénédicte Fruneau[12]

Abstract

We report a rarely observed case of steady aseismic deformation in the context of a fold-and-thrust belt, with a well-documented structural and lithological background. We focus on a 12-km-long section across the foothills of southwestern Taiwan, where about 23 mm/yr of westward compression is observed. From west to east, the surface geological structures include an anticline, a thrust and a backthrust. We determine Holocene uplift rates based on fluvial terraces, invert the interseismic 3D velocity field using existing geodetic datasets, and build a geological cross-section to constrain the possible deep geometry for the structure responsible for the observed surface deformation. Geodetic vertical velocities and Holocene uplift rates show a similar pattern, with rates rapidly increasing eastward, then remaining relatively constant across the fold axis and thrust, and finally sharply decreasing across the backthrust, across which InSAR (Interferometric Synthetic Aperture Radar) observations suggest a velocity discontinuity. Our observations show that active deformation is occurring mainly aseismically and involves the anticline and backthrust. Our cross-section illustrates a 4–5 km deep wedge with a passive roof thrust corresponding to the backthrust, on the hanging wall of which the anticline is located. A classical fault-bend fold model with a slip rate of 21 ± 2 mm/yr can explain most of the observations, yet local misfit suggests a possible contribution to uplift from pure shear of clayey rocks in the anticline core. Based on published records from a deep well drilled across the fold core and backthrust, clay-rich lithology and elevated fluid content are likely to favor aseismic slip.

Keywords Seismic cycle, Fault creep, Fold growth, Fault-related folding, Folded fluvial terraces

---

*Correspondence:
Maryline Le Béon
mlebeon@g.ncu.edu.tw
[1] Graduate Institute of Applied Geology, National Central University, Taoyuan, Taiwan
[2] E-DREAM (Earthquake-Disaster and Risk Evaluation and Management Center), National Central University, Taoyuan, Taiwan
[3] Department of Earth Sciences, National Central University, Taoyuan, Taiwan
[4] Department of Geomatics, National Cheng Kung University, Tainan, Taiwan
[5] Now at Department of Earth Sciences, National Taiwan Normal University, Taipei, Taiwan
[6] Now at Sinotech Engineering Consultants, Tld., Taipei, Taiwan
[7] GSMMA (Geological Survey and Mining Management Agency), Ministry of Economic Affairs, New Taipei City, Taiwan
[8] Department of Earth and Environmental Sciences, National Chung Cheng University, Chiayi, Taiwan
[9] Univ. Grenoble Alpes, Univ. Savoie Mont Blanc, CNRS, IRD, Univ. Gustave Eiffel, ISTerre, 38000 Grenoble, France
[10] Department of Earth Sciences, National Cheng Kung University, Tainan, Taiwan
[11] Research Center for Environmental Change, Academia Sinica, Taipei, Taiwan
[12] LaSTIG, Université Gustave Eiffel, Champs-Sur-Marne, France

Introduction

Distinctive modes of slip were reported on faults, namely frictional slip instabilities that radiate seismic waves (earthquakes) and stable sliding (or aseismic slip) that generate little to no (or undetectable) seismicity and may occur as transient postseismic afterslip, transient slow-slip events, or as steady interseismic fault creep (see Avouac (2015) for a review). Recognizing and further understanding aseismic slip occurring on a fault is essential as it limits the amount of elastic strain stored in the crust around the fault and lowers the associated seismic hazards, although faults with creeping segments were witnessed to produce $M_w > 6$ earthquakes (Chen and Bürgmann 2017; Harris 2017). Factors promoting aseismic slip include clay-rich material, high pore pressure, elevated temperature, or a combination of all (Avouac 2015; Harris 2017).

Most of the creeping faults identified in continental settings are strike-slip faults (e.g., Chen and Bürgmann 2017; Harris 2017). Surface creep is commonly recognized based on gradual damage to man-made structures built across fault traces and thanks to geodetic techniques. These techniques tend to perform better on horizontal deformation, in areas with limited topography and vegetation, so that creep on dip-slip faults may be harder to detect. Besides, dip-slip faults, in particular thrust faults, may be blind, buried under recent deposits or colluvial wedges, so that creep on such faults would lead to distributed deformation at the surface. Nevertheless, a literature review of aseismic slip in continental compressional settings led to a fair number of cases, yet only a minority are classified as steady interseismic creep. In the context of the eastern Taiwan accretionary wedge, steady creep was documented on the Chihshang Fault based on InSAR and ground-based geodesy, with the clay-rich Lichi Mélange proposed as the promoting factor (Thomas et al. 2014a, 2014b). In the southwestern Taiwan Coastal Plain, a sharp deformation gradient identified in geodetic observations was attributed to the creeping Houchiali Fault, rooted in clay-rich and likely overpressured bedrock, and which tip appears to be buried in Holocene sediments (Huang et al. 2009; Le Béon et al. 2019). Last, in the volcano-tectonic context of Mount Etna (Sicily), InSAR and a possibly folded Holocene lava flow suggested aseismic fold growth due to slip on a thrust rooted within a clay-rich sedimentary sequence (Bonforte et al. 2011; De Guidi et al. 2015). Other studies reported creep events that appear to be associated with local or regional earthquakes. A series of studies mainly based on InSAR and seismicity identified aseismic deformation attributed to thrusts associated with transpression along large strike-slip faults. Surface deformation followed earthquakes on strike-slip faults or deeper thrusts within the same transpressional fault systems, located in eastern Iran (1998 M_w6.6 Fandoqa, Shahdad fold-thrust belt, Fielding et al. (2004), Copley and Jolivet (2016); 1994 Sefidabeh sequence, Copley and Reynolds (2014); 1978 M_w7.3 Tabas, Zhou et al. (2016)), in southern Tarim (China) (2013 M_w6.3 Pishan, Ainscoe et al. (2017)) and eastern Turkey (2011 M_w7.1 Van, Mackenzie et al. (2016)). At last, in the context of fold-and-thrust belts, aseismic slip also following earthquakes was proposed on thrusts of the Simply Folded Belt of Zagros (Iran) (2005 M_w5.9 Qesm and 2006 M_w5.9 Fin, Barnhart and Lohman (2013); 2003–2011 sequence, Barnhart et al. (2013); 2013 M_w6.2 Khaki-Shonbe, Elliott et al. (2015)) and on structures of the southwestern Taiwan fold-thrust belt (2016 M_w6.4 Meinong, Huang et al. (2016), Lu et al. (2024)). Among these postseismic studies, aseismic deformation prior to the earthquakes was recognized in the Shahdad and southwestern Taiwan fold-thrust belts (Copley and Jolivet 2016; Le Béon et al. 2017), where detachments, respectively, lie within salt formation and overpressured mudstone.

This study documents Holocene and interseismic deformation within the Western Foothills of the southern Taiwan fold-thrust belt, across a complex structure including a major geological thrust with a backthrust on its hanging wall and an anticline on its footwall. We bring together Holocene uplift rates constrained by fluvial incision, deformation rates based on geodetic techniques, and a balanced geological cross-section. We discuss the possible structural model and modes of slip responsible for the observed deformation, as well as the factors that favor aseismic deformation and the implications for seismic hazards.

Geological and tectonic setting

The Taiwan mountain belt results from the rapid collision, started 5–7 Ma ago, between the Luzon volcanic arc on the Philippine Sea Plate and the Eurasian passive margin (e.g., Suppe 1984; Lee et al. 2015; Fig. 1). Active shortening occurs across the plate suture zone in eastern Taiwan and across the mountain piedmont in the west, called the Western Foothills (e.g., Hsu et al. 2009; Shyu et al. 2020). In our study area, in the foothills of southern Taiwan, GNSS measurements indicate about 35 mm/yr of westward (N285°) shortening from Yuching town to the coastline about 40 km west (Ching et al. 2018; Fig. 1). The most significant geological structure is the Lunhou Fault (also called Chukou Fault) that brought Late Miocene to Early Pliocene passive margin strata above younger foreland basin Pliocene formations (CPC, 1989; Ho et al. 2005; Fig. 1). Its hanging wall hosts the Kouhsiaoli Fault, which has a smaller separation, and the Yuching Syncline with Late

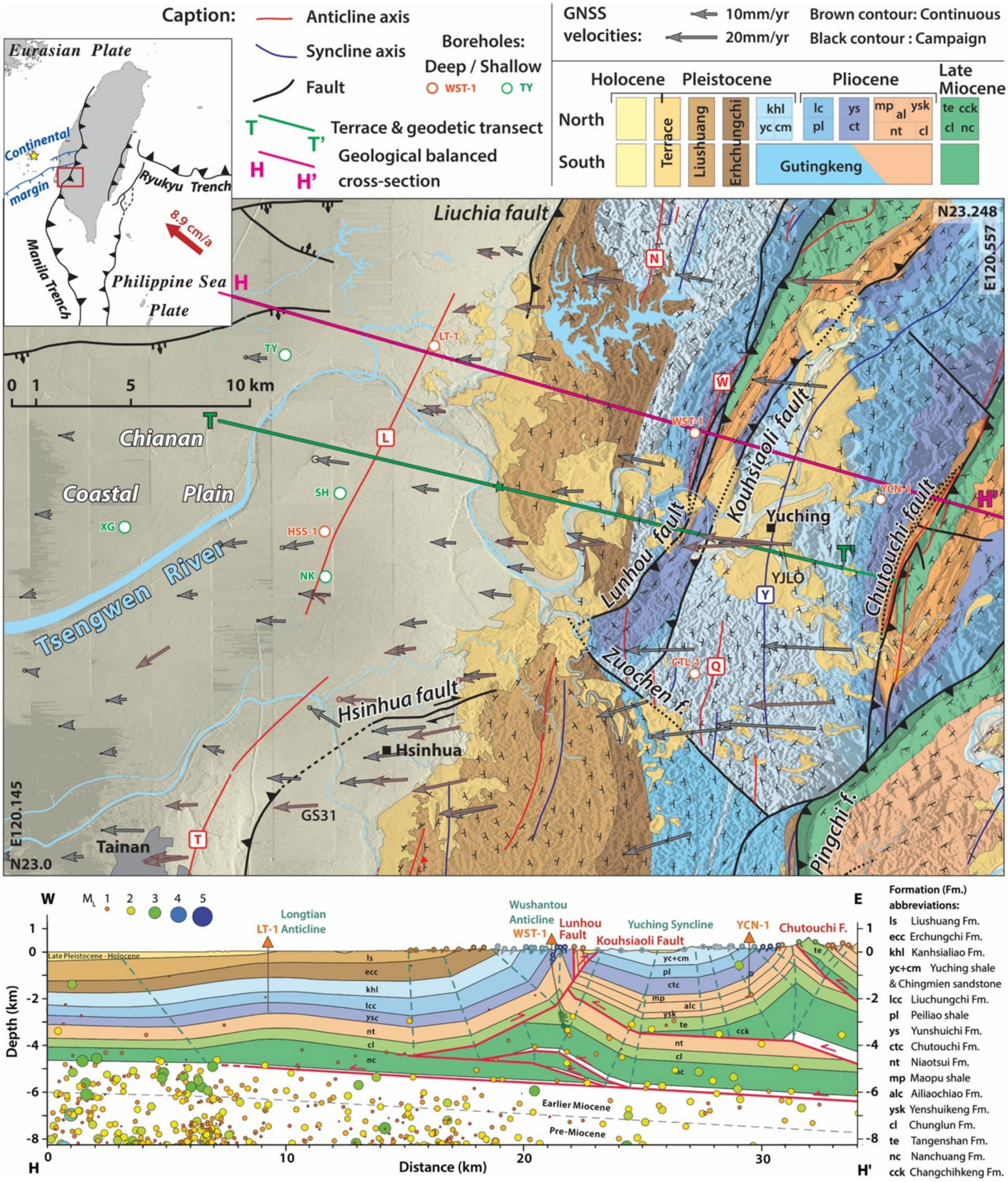

Formation (Fm.) abbreviations:

- **ls** Liushuang Fm.
- **ecc** Erchungchi Fm.
- **khl** Kanhsialiao Fm.
- **yc+cm** Yuching shale & Chingmien sandstone
- **lcc** Liuchungchi Fm.
- **pl** Peiliao shale
- **ys** Yunshuichi Fm.
- **ctc** Chutouchi Fm.
- **nt** Niaotsui Fm.
- **mp** Maopu shale
- **alc** Ailiaochiao Fm.
- **ysk** Yenshuikeng Fm.
- **cl** Chunglun Fm.
- **te** Tangenshan Fm.
- **nc** Nanchuang Fm.
- **cck** Changchihkeng Fm.

Fig. 1 Regional geological map of the Tsengwen River area and geological cross-section HH′. Map was compiled from Chinese Petroleum Corporation (CPC) (1989), active faults in Taiwan (Central Geological Survey, 2021), and Le Béon et al. (2017). Fold axes: *T*=Tainan anticline; *L*=Longtian anticline (Hsinying in Le Béon et al. (2017)); *N*=Niushan anticline; *W*=Wushantou anticline; *Q*=Chiutsenglin anticline; *Y*=Yuching syncline. Horizontal GNSS velocities (2016–2021) are from Ching et al. (2021) with reference to station S01R on Penghu Islands (yellow star in inset map). Dashed black rectangle shows the study area (Fig. 2). Green star indicates kilometer 12 along TT′ for convenience in locating transects shown in Figs. 4 and 7. Relocated seismicity during 1990–2020 is superimposed on the cross-section. This catalogue is updated from Wu et al. (2008) catalogue, using the velocity model of Wu et al. (2009), and available at http://seismology.gl.ntu.edu.tw/. Inset map shows the background tectonic setting, with main normal faults of the passive margin from Lin et al. (2003) and Yang et al. (2016) and plate convergence rate from Argus et al. (2011)

Pliocene to Early Pleistocene rocks along its axis. Prior to this study, it was unclear whether the Lunhou and Kouhsiaoli Faults are active. West of the Lunhou Fault, bedding dips are steep along the Wushantou Anticline fold axis and become progressively shallower westward. The Plio-Pleistocene foreland basin sequence evolves from clay-rich facies of the Middle to Late Pliocene Yunshuichi and Chutouchi Formations to sandier Late Pleistocene facies, capped with Holocene marine and alluvial sediments in the Coastal Plain (e.g., Chen et al. 2001, 2004; Hsieh et al. 2006). There, the buried Longtian Anticline is identified based on deep seismic reflection profiles (Hu and Sheen 1989).

The Tsengwen River is one of the most significant westward-flowing rivers. It crosses the geological structures mentioned above and left fluvial terraces as relicts of its paleo-riverbed (Figs. 1 and 2). Hsieh and Knuepfer (2002) identified fluvial terraces preserved at higher elevations near the Wushantou Anticline axis compared to upstream and downstream the anticline. Radiocarbon dating of the Late Holocene lower terrace levels provided hints for active uplift due to the growing anticline. In this study, we expand the radiocarbon dataset of Hsieh and Knuepfer (2002) and complement Holocene observations with geodetic observations and a structural analysis to further characterize active deformation.

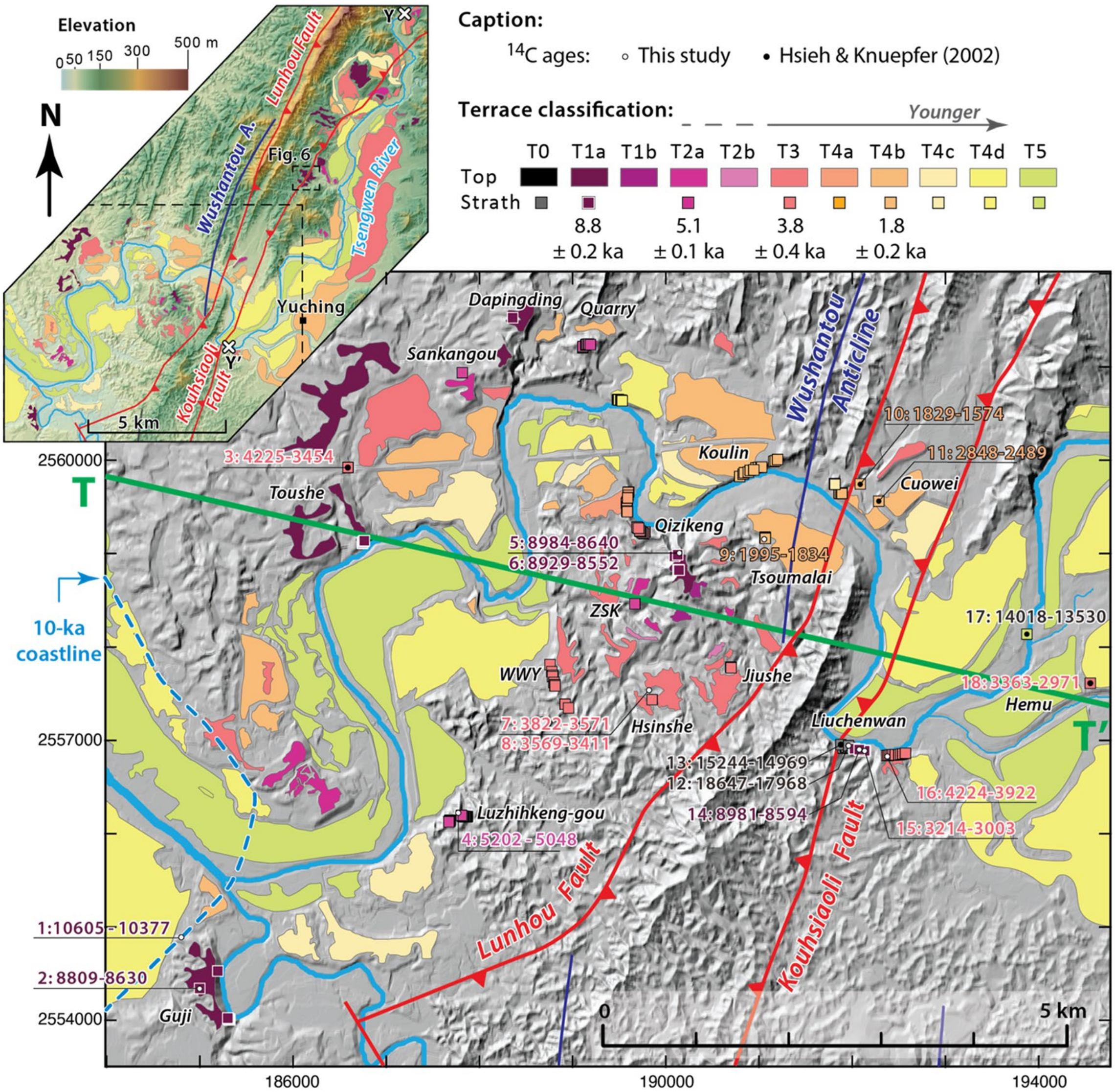

Fig. 2 Map of the Tsengwen River terraces. Inset map location is shown in Fig. 1. Terrace longitudinal profile TT' is shown in Fig. 4. 5-m shaded DEM is utilized for the background. The 10-ka coastline is from Chen et al. (2004). Fault traces are from Huang et al. (2020) and fold axes from CPC (1989). Coordinates are Taiwan grid TW97/TM2 in meters (https://epsg.io/3826)

Data and methods

Field observations and mapping of the Tsengwen River terraces

Topographic data and field survey

Geomorphic analyses are based on a 5-m DTM (Digital Terrain Model) derived from aerial photographs, a 1-m DTM based on airborne LiDAR data, and a 20-m DTM resampled from the LiDAR DTM. A UAV (unmanned aerial vehicle) was used to acquire images (processed using Pix4D) of inaccessible outcrops and to produce local Digital Surface Models (DSM) and orthoimages of outcrops along the riverbed or cliffs, with a 2-cm to 5-cm resolution. When possible, the processing included a minimum of 3 ground control points per site, with their positions measured using a VBS-RTK (Virtual Base Station Real-Time Kinematic) GNSS apparatus. Terrace deposits, strath contacts, and radiocarbon sample positions were surveyed using a total station, VBS-RTK GNSS, UAV 3D models or measuring tape depending on the setting of the sites. Uncertainties on elevations relative to the modern river were estimated according to measurement method and accounted for wavy bedrock strath when observed. They range from 0.5 to 4 m.

Radiocarbon ages, terrace mapping and correlation

Alluvial geomorphic surfaces were identified based on shaded DTMs, slope maps and topographic contour lines and validated in the field (Fig. 3). Terrace surfaces were correlated by comparing their elevations relative to the modern river, or height, with the height of surfaces within close distances and on the same side of a fault. Correlations between distant terrace surfaces or across faults were established thanks to radiocarbon ages. Terraces with non-preserved geomorphic surfaces were mapped based on exposed terrace deposits and strath.

Radiocarbon samples were prepared and measured at the Beta Analytic or National Taiwan University Acceleration Mass Spectrometry facilities. Conventional ages newly obtained in this study and published ages from Hsieh and Knuepfer (2002) and Liu et al. (2020) were calibrated using the IntCal20 calibration curve (Reimer et al. 2020) (Table 1, Data Set 1).

Radiocarbon samples were collected at any depth within the deposits, including within silty material near the terrace top, which likely deposited during floods shortly before or after terrace abandonment. Besides, the samples consist of different materials (wood, charcoal, or plant remain) that have different sensitivity to recycling. Hence, for terraces constrained by several ages, we consider the entire period covered by all ages and their 2-sigma uncertainty to determine a single depositional age for each terrace level, which will be used for incision rate calculations (Fig. 2, Table 2). For T1a, we considered samples 2, 5, 6 and 14 to set a depositional age of 8.6–9.0 ka B.P. For T3, samples 3, 7, 8, and 16 lead to an age of 3.4–4.2 ka B.P., excluding sample 15 (3.0–3.2 ka B.P.) as it is the youngest and only sample of T3 collected in overbank deposits. For T4b, samples 9 and 10 define an age of 1.6–2.0 ka B.P., excluding sample 11 (2.5–2.8 ka B.P.) as justified in Sect. "Qualitative evidence from fault outcrops and river terraces along transect TT’". Depositional ages underestimate the formation age of bedrock straths, hence overestimate bedrock incision rates.

Determination of Holocene uplift rates

Rates relative to the coastal plain

Bedrock straths capped by dated fluvial deposits allow quantifying bedrock incision rates that result from the combined effects of local and regional tectonic uplift and changes in the river base level (sea-level change, basin filling), sinuosity and gradient (Lavé and Avouac 2000). We consider river sinuosity and gradient constant during the Holocene (more in Sect. "Qualitative evidence from fault outcrops and river terraces along transect TT’"). However, base level changes likely affected the Tsengwen River in our study area. Following rapid regional sea-level rise after the Last Glacial Maximum (e.g., Lambeck et al. 2014), the coastline was reported at the toe of the foothills at the early Holocene (Fig. 2) and later migrated westward due to sedimentary filling (Chen et al. 2004; Hsieh et al. 2006). To account for it, we determine sedimentation rates in the Coastal Plain using published radiocarbon dates of buried strata at four shallow borehole sites (green dots in Fig. 1; Table S1). Linear regression and 95% confidence interval provide an average sedimentation rate for each period equivalent to a terrace age (Figure S1). Eventually, Holocene uplift rates (Table 2) are calculated relative to the Coastal Plain by adding bedrock incision rates and Coastal Plain sedimentation rates.

Rates derived from paleosea-level

Stratigraphic observations at the Guji site (location in Fig. 2; Fig. 3d) indicate a coastal depositional environment (more details in Sect. "Qualitative evidence from fault outcrops and river terraces along transect TT’"). Hence, these layers can be used to quantify uplift based on paleosea-level. Uplift is calculated by subtracting the current elevation of the dated layer and the elevation of sea-level at the time of layer deposition, taken from the paleosea-level curve of Chen et al. (2020). We assume an uncertainty of 2 m on the paleo-environment water depth (Table S2).

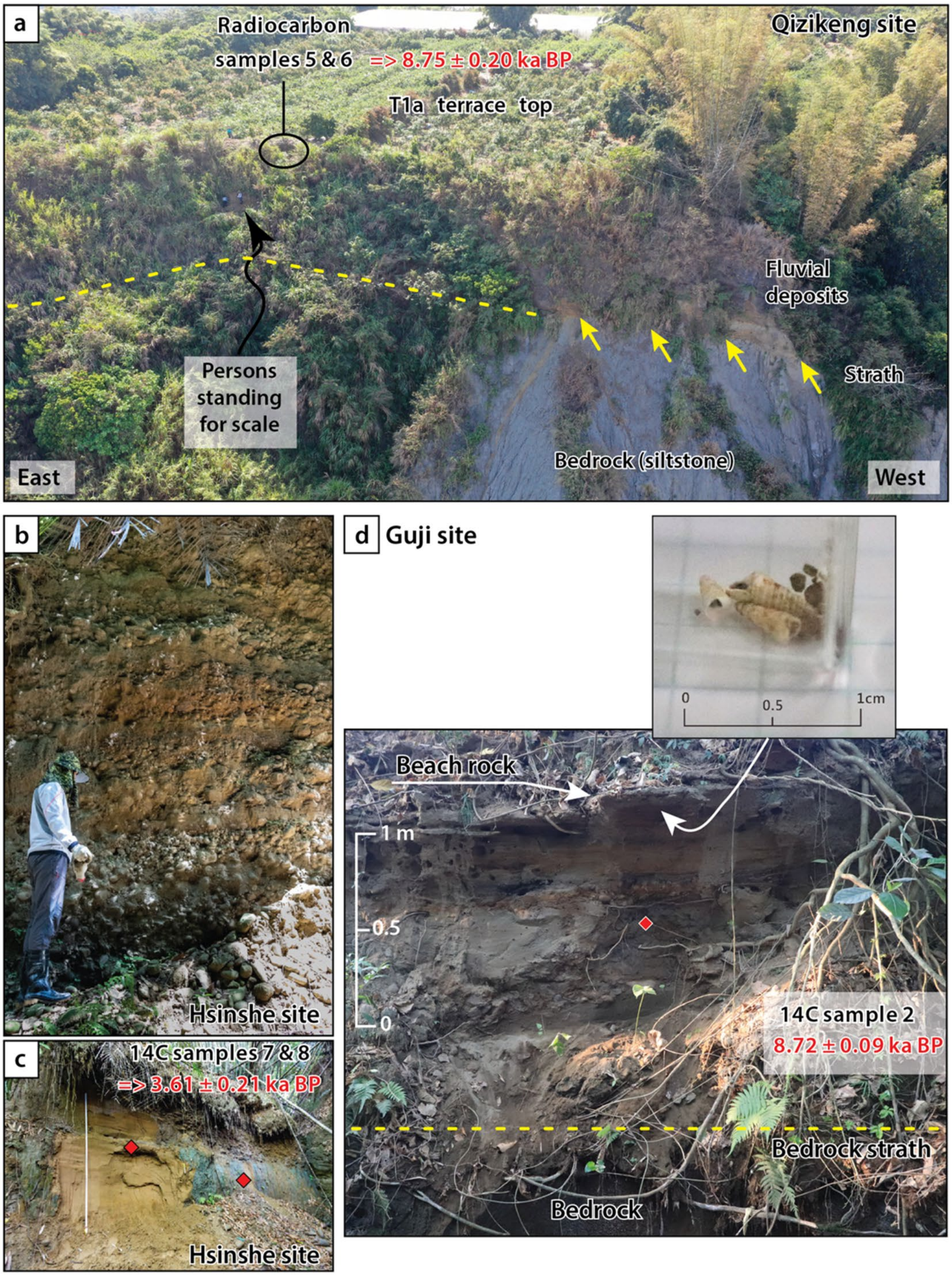

Fig. 3 Examples of field observations of the Tsengwen River terrace deposits. See Fig. 2 for sites location. Deposits consist of gravel layers and coarse- or medium-grained sand layers, often laminated, and commonly capped with silt or clayey silt. **a** Drone view of the highest terrace T1a (Qizikeng site), with strath and ^{14}C sampling site. **b**–**c** Observations of fluvial facies of terrace T3 deposits (Hsinshe site): alternating conglomerate and sand (**b**) and laminated sand layers containing dated charcoals (**c**). **d** Observations of fluvio-marine deposits above bedrock strath at ^{14}C sampling site 2 (Guji site), indicating a former coastal environment. Numerous marine shells were found under the beach rock roof

Table 1 Radiocarbon ages from the Tsengwen River terrace deposits (see location in Fig. 2). More detailed information is provided in Table S1

Sample number (1)	Terrace level	Sample type and occurrence (2)	Strath elevation (m)	Sample elevation (m)	Conventional age (yr B.P.)	Calibrated age (2σ cal B.P.) (3)
Guji						
1*	T1a	C/Lam. fS (RC)	< 27 ± 1	33.6 ± 0.2	9320 ± 40	10605–10377
2*	T1a	C/Cl. Ls. (RC)	46.9 ± 0.5	48.4 ± 0.3	7920 ± 30	8890–8630
Toushe						
3#	T3	P/OB	39 ± 2.5	47 ± 2.5	3520 ± 140	4224–3454
Luzhihkeng-gou						
4*	T2a	C/Lam. fS (RC)	88.6 ± 0.5	98.7 ± 0.3	4510 ± 30	5202—5048
Qizikeng						
5*	T1a	C/Si. fS (OB)	151.5 ± 1.5	162.8 ± 0.3	7940 ± 30	8984–8640
6*	T1a	C/Si. fS (OB)	151.5 ± 1.5	162.7 ± 0.3	7870 ± 30	8929–8552
Hsinshe						
7*	T3	C/Lam. mS (RC)	85 ± 1	87.5 ± 0.5	3420 ± 30	3822–3571
8*	T3	C/Lam. mS (RC)	85 ± 1	87.3 ± 0.5	3280 ± 30	3569–3411
Tsoumalai						
9*	T4b	C/fS (RC)	54.5 ± 1.5	64.9 ± 0.2	1990 ± 30	1995–1834
Cuowei						
10#	T4b	W/G (RC)	70 ± 2.5	70 ± 2.5	1810 ± 50	1829–1574
11#	T4b	W/G (RC)	67 ± 2.5	67 ± 2.5	2590 ± 60	2848–2489
Liuchenwan						
12*	T0	W/G (RC)	61.2 ± 0.2	61.4 ± 0.2	14950 ± 120	18647–17968
13$	T0	W/G (RC)	61.2 ± 0.2	61.4 ± 0.2	12670 ± 40	15244–14969
14*	T1a	P/Cl. Ls. (RC)	60.1 ± 0.4	66.1 ± 0.2	7900 ± 40	8981–8594
15*	T3	C/Mo. Si. (OB)	55.8 ± 0.2	66.7 ± 0.2	2960 ± 30	3214–3003
16*	T3	C/Si. fS (OB)	49.3 ± 0.3	53.0 ± 0.5	3710 ± 40	4224–3922
Hemu						
17#	R	W/G (RC)	37 ± 2.5	41 ± 2.5	11900 ± 70	14018–13530
18#	T3	P/OB	55. ± 2.5	57 ± 2.5	3001 ± 67	3363–2971

(1): numbers are also indicated in Fig. 2 and Table S1; oblique font names are site names, also shown in Fig. 2; symbols indicate the source of the age data: * = this study; # = Hsieh and Knuepfer (2002); $ = Liu et al (2020)

(2): sample type/occurrence: for sample type: C = charcoal, P = plant remain; occurrence refers to sediment description and facies: Cl. = clayey, Si. = silty or silt, fS = fine sand, mS = medium sand, G = gravel, Ls = lens, Lam. = laminated, Mo. = mottled; (RC) = river channel facies, (OB) = overbank flood deposit

(3): calibration based on IntCal20 (Reimer et al. 2020)

Geodetic datasets and velocity field inversion

Present-day surface velocities come from three different geodetic datasets. The horizontal and vertical velocities during 2016–2021 are provided by the Geological Survey and Mining Management Agency (Ching et al. 2021; Data Set 2), relative to station S01R in Penghu Island (yellow star in Fig. 1, inset map). Data from 11 continuous and 24 campaign-mode GNSS stations, and from 28 benchmarks on three leveling routes are used. Horizontal velocities are derived from continuous and campaign-mode GNSS data, and vertical velocities from continuous and campaign-mode GNSS and precise leveling data. Data acquisition and processing are as described in Ching et al. (2016).

The ascending ALOS-1 line-of-sight (LOS) velocities (Data Set 3; Figure S3) are derived from a time-series analysis during 2007–2011 based on a small baseline approach (NSBAS (New Small BAseline Subset) method; Doin et al. 2011; Minh et al. 2022), including atmospheric correction using European Centre for Median Range Weather Forecast reanalysis model and LOS correction using GNSS data (Pathier et al. 2014; Fruneau et al. 2017). The ascending and descending Sentinel-1 LOS velocities during 2016–2018 are estimated using the Persistent Scatterer InSAR (PSInSAR) processing (Lu 2022; Lu et al. 2024; Figure S3). Next, the ascending and descending LOS velocities are decomposed into EW and vertical components. To compare them with the GNSS and

Table 2 Uplift rates relative to the Coastal Plain based on Tsengwen River strath terrace observations, bedrock river incision rates and Coastal Plain sedimentation rates (site locations in Fig. 2)

Site Name (1)	Age flag (2)	Average Location of strath observations	Strath Elevation (m)	Strath Height (m)	Bedrock incision rate (mm/yr)	Relative uplift rate (mm/yr) (3)
Guji T1a: E cliff and Sample 2	Dated	185012/2554358	46.9 ± 0.5	36.9 ± 0.5	3.9 ± 0.5	7.9 ± 0.9
Guji T1a: W gully and Sample 1*	Dated	184807/2554895	< 27 ± 1	< 17 ± 1	< 1.8 ± 0.3	< 5.8 ± 0.7
Toushe T3	Dated	186592/2559921	39 ± 2.5	28 ± 2.5	7.5 ± 1.5	10.6 ± 1.7
Toushe T1a?	Correl	186704/2559219	55 ± 1	43 ± 1	4.6 ± 0.6	8.5 ± 1.0
Sankangou T2a?	Correl	187819/2560935	72 ± 1	57 ± 1.5	11.1 ± 0.5	15.1 ± 0.9
Dapingding T1a?	Correl	188374/2561518	104.6	89.6 ± 0.5	9.5 ± 1.0	13.5 ± 1.4
LuzhihKG # T2a	Dated	187775/2556227	90 ± 1	82.0 ± 1.5	16.0 ± 0.5	20.0 ± 0.9
Quarry T2a?	Correl	189151/2561197	97.8 ± 1.9	80.8 ± 2.4	15.8 ± 0.7	19.7 ± 0.9
WWY # T3?	Correl	188810/2557597	82.5 ± 1.0	69.5 ± 1.5	18.5 ± 2.4	21.6 ± 2.6
Qizikeng T3	Correl	189704/2559272	86.5 ± 1.6	66.5 ± 1.6	17.7 ± 2.1	20.8 ± 2.5
ZSK # T2a?	Correl	189701/2558479	109 ± 0.5	89 ± 0.5	17.4 ± 0.4	21.3 ± 0.6
Qizikeng T1a	Dated	190144/2559004	151.5 ± 1.5	131.5 ± 1.5	13.9 ± 1.7	17.9 ± 2.0
Hsinshe T3	Dated	189819/2557540	85 ± 1	65 ± 1	17.3 ± 2.1	20.4 ± 2.3
Jiushe T3	Correl	190698/2557785	93.0 ± 1.5	73.0 ± 1.5	19.4 ± 2.5	22.5 ± 2.7
Koulin T4b	Correl	191026/2559924	58.5 ± 1.5	37.5 ± 1.5	21.4 ± 3.4	24.5 ± 3.6
Tsoumalai T4b	Dated	191053/2559153	54.5 ± 1.5	34.5 ± 1.5	19.7 ± 3.2	22.8 ± 3.4
Cuowei T4b: W of Sample 10	Correl	191876/2559924	58.5 ± 1.8	33.5 ± 1.8	19.2 ± 3.4	22.3 ± 3.6
Cuowei T4b: Sample 10 area	Dated	192081/2559745	70 ± 2.5	45 ± 2.5	25.7 ± 4.4	28.8 ± 4.6
Cuowei T4b: Sample 11 area	Dated	192281/2559560	67 ± 2.5	42 ± 2.5	24.0 ± 4.2	27.1 ± 4.4
Liuchenwan T0	Dated	191945/2556925	59.5 ± 0.5	29.5 ± 0.5	1.8 ± 0.2	9.7 ± 1.2
Liuchenwan T1a	Dated	192072/2556904	54 ± 4	24 ± 4	2.6 ± 0.7	6.6 ± 1.1
Liuchenwan T3	Dated	192372/2556830	49 ± 1	19 ± 1	5.1 ± 0.8	8.2 ± 1.0
Hemu T3	Dated	194547/2557614	55 ± 2.5	13 ± 2.5	3.5 ± 1.0	6.6 ± 1.2

(1) * = strath elevation is lower than the bottom of gullies incised within the western part of the terrace; # = LuzhihK.G., WWY and ZSK stand for Luzhihkeng-gou, WaiwuYing and Zhuoshuikeng, respectively. Question marks after site names indicate low-confidence level in the terrace correlation

(2) "Correl." stands for correlated: terrace was not dated at this site, but correlated based on relative elevation and map-view pattern

(3) Calculated as bedrock incision rate (i.e., strath height above the modern river divided by terrace age) minus Coastal Plain sedimentation rate. Terrace ages (in yr B.P.) are as follows: [14969, 15244] for T0, [8552, 10605] for T1a, [5048, 5202] for T2, [3411, 4225] for T3, and [1574, 1995] for T4b. Sedimentation rates are as follows: 7.8 ± 1.0 mm/yr for T0, 4.0 ± 0.4 mm/yr for T1a, 3.9 ± 0.2 mm/yr for T3, and 3.1 ± 0.2 mm/yr for T4b (Figure S1)

leveling vertical velocities, LOS dataset and EW and vertical components were calculated in reference to GNSS station S01R. Complementary information on the processing is provided in Supplementary Text S1.

We performed an inversion to integrate the different geodetic datasets in a single 3D velocity field, thereby achieving a more comprehensive and accurate depiction of surface deformation. Information on the inversion method is summarized here and described in more details in Supplementary Text S2. Wang and Wright (2012) and Walters et al. (2014) proposed using a triangular mesh for linear interpolation to combine high-precision three-component GNSS observations and widely distributed InSAR single-component observations to derive the three-component velocity field of the study area. This method divides the study area into Delaunay triangular grids and assumes that the velocity field changes linearly along latitude and longitude. Thus, the relationship between any observation point within the grid and the three nodes of the grid can be expressed by a linear interpolation formula, called the shape function. The Laplacian smoothing operator is also used to obtain a reasonable, smooth inferred velocity field. In this study, we further modified the equations proposed by Wang and Wright (2012) and Walters et al. (2014). First, the leveling vertical velocity is included in the inversion. Then, because of the ionospheric disturbances or other unknown factors causing discrepancies between GNSS LOS velocity and InSAR LOS velocity, the long-wavelength noise correction proposed by Tsukahara and Takada (2018) is applied to calibrate the InSAR LOS velocities. In addition, we also allow the presence of surface velocity discontinuity across a fault trace inferred to creep near the ground surface. This is achieved by removing the Delaunay triangles that cross the creeping fault. Finally, we adopted 10,000 samples for the bootstrap method to estimate the uncertainty of the derived 3D velocity field (Figure S5).

We determine the 3D velocity field by inverting the geodetic datasets presented above using the modified velocity inversion method that includes a discontinuity across the Kouhsiaoli Fault trace. We first inverted separately the ALOS-1, GNSS and leveling datasets to produce a velocity field for the period 2007–2021, and the Sentinel-1, GNSS and leveling datasets to obtain a velocity field for the period 2016–2021. Since the results were consistent with each other (Figure S5), we eventually inverted the entire dataset to obtain a velocity field for the period 2007–2021.

Geological cross-section

To understand the origin of ground surface deformation, we built the balanced geological cross-section HH' (Fig. 1). It is constrained by attitudes of bedding and fault planes from published geological maps (CPC, 1989; Ho et al. 2005) and our own field measurements, by stratigraphic constraints within the Coastal Plain derived from a dense network of seismic reflection profiles and deep boreholes (Hu and Sheen 1989), and by deep boreholes with the foothills (Hsieh and Liu 1971; Huang et al. 2004; Fig. 1). The cross-section is drawn following the kink method and principles of fault-bend folding, as well as detachment folding (Suppe 1980, 1983; Shaw et al. 2005).

Results

Holocene tectonic activity

Qualitative evidence from fault outcrops and river terraces along transect TT'

From the Guji site to the Lunhou Fault (Figs. 2 and 4), ten terrace levels are identified and labeled T1a (8.6–9.0 ka B.P.) to T5 (<2 ka), from oldest to youngest, indicative of sustained river incision in this area. The depositional sequences are 4 to 24 m thick, commonly capped with silt or clayey silt interpreted as flood deposits. The terrace map displays evidence for the sinuous morphology of the paleo-Tsengwen River, with curved terrace risers and terraces that are progressively lower towards the inner part of meanders. The map-view pattern of the T3 terraces west of the Lunhou Fault likely corresponds to a cut-off meander. The highest terrace T1a is found at Qizikeng where the bedrock strath lies about 90 m above the modern river (Fig. 4; Table 1). By comparison, the bedrock strath beneath T3 at Hsinshe and T4 at Tsoumalai, respectively, lies 65 m and 35 m above the modern river. Meanwhile, downstream, at Guji and Toushe, the bedrock strath height beneath T1a and T3 is only 35 and 25 m, respectively, which indicates faster river incision in the Qizikeng–Hsinshe area compared to the Guji–Toushe area.

At Guji, we observed a 24-m-thick sedimentary sequence comprising sandy layers with shell fragments or complete shells and indurated sand layers with authigenic carbonate crystals, interpreted as beach

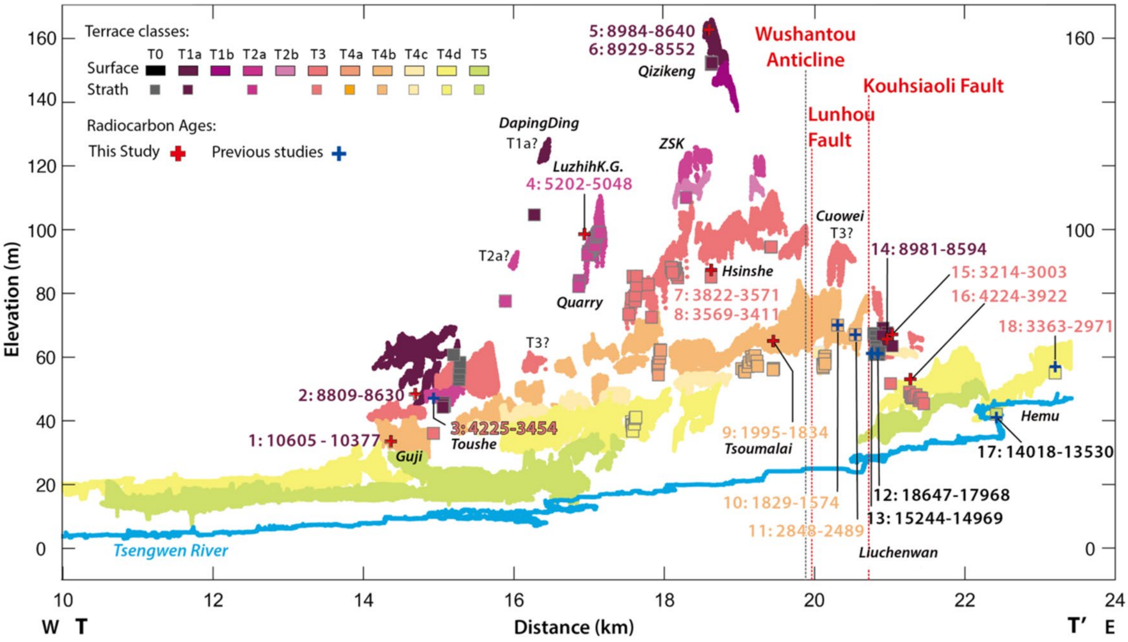

Fig. 4 Terrace and river longitudinal profiles projected along TT' (location in Figs. 1 and 2). Radiocarbon ages and strath observations are presented in Tables 1 and 2 and in Data Set 1

rock (Fig. 3d). The sequence rests on top of an irregular bedrock strath, lying deeper than the lowest channels (< 27 m elevation) in the north and west, and exposed at 44.3–46.9 m elevation in the center and east. Charcoals gave radiocarbon ages of 10.4–10.6 ka B.P. (sample 1) near the base of the sequence and 8.6–8.8 ka B.P. (sample 2, collected above the strath; Fig. 3d) near the top. Our observations suggest a Late Pleistocene paleotopography, covered by Early Holocene transgressive fluvio-marine sediments (probably deltaic), in agreement with the location of the 10-ka coastline of Chen et al. (2004) (Fig. 2).

Between the Lunhou and Kouhsiaoli faults, sublevels of terrace T4 are mainly observed. Correlation across the Lunhou Fault is ensured by radiocarbon ages at Tsoumalai (sample 9, 1.8–2.0 ka B.P.) and Cuowei (sample 10, 1.6–1.8 ka B.P.). Because of the clear difference between T3 and T4 terraces (elevation and river path), sample 11 dated 2.5–2.8 ka B.P., i.e., closer to T3 ages than to samples 9 and 10, is considered as reworked. Terrace T4b lies at similar elevation across the Lunhou Fault, showing that the fault activity has been little to none in the last 2 ka. An undated terrace observed north of Cuowei is diffidently mapped T3 and excluded from uplift rate calculations.

Between the Kouhsiaoli Fault and Hemu, geomorphic surfaces were mainly assigned T4d and T5 based on their low heights (25–30 m and 15 m). At Liuchenwan, a long cliff on the southern river bank exhibits river deposits capping a bedrock strath which elevation increases step-wise towards the fault. At sample site 16 (3.9–4.2 ka B.P.), terrace deposits classified as T3 cap a sub-horizontal strath with 15–18 m height. Further west (Fig. 5a), beneath samples 14 (8.6–9.0 ka B.P.) and 15 (3.0–3.2 ka B.P.), the strath height is 33 m at its lowest point. Sample 14 is a plant fragment (unlikely to be reworked) and lies at lower elevation than sample 15, thus we infer that the strath formed prior to deposition of sample 14, equivalent to T1a, and that T1a deposits were covered by T3 deposits, probably during flooding, since sample 15 was found in silt. To the west, strath increases in elevation. At its lowest point, 29 m above the modern river, wood samples 12 (18.0–18.6 ka B.P.) and 13 (15.0–15.2 ka B.P.) were found within a conglomerate just above the strath and considered as T0 deposits. Our observations along this cliff point to a relatively stable riverbed since

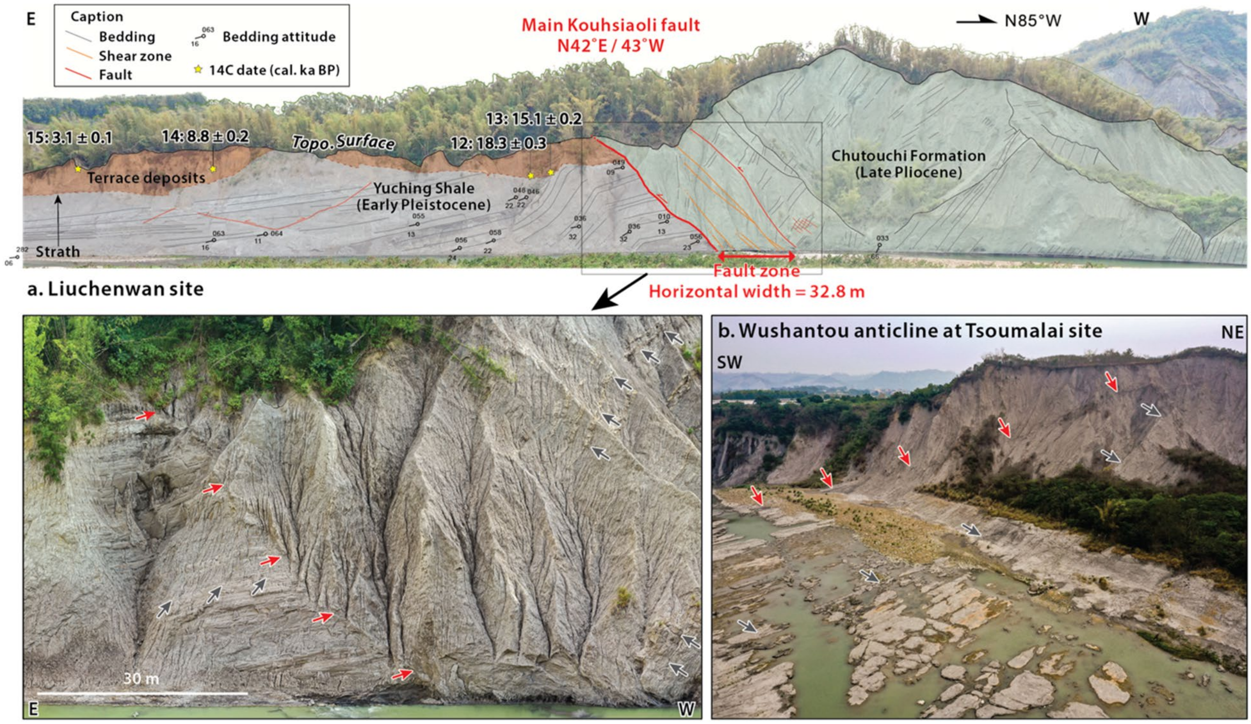

Fig. 5 **a** Outcrop of the Kouhsiaoli backthrust fault zone at the Liuchenwan cliff site (location in Fig. 2). The active backthrust dips 43°W and brings steeply *E*-dipping Late Pliocene rocks on top of < 18-ka terrace deposits and Early Pleistocene strata dipping to the E at a shallow angle. Footwall terrace deposits and ages are interpreted as a sequence of periods of limited bedrock incision and fluvial deposition. On the lower left panel, grey arrows point bedding and red ones the main fault contact. **b** Drone view of the west limb of the Wushantou anticline (Tsoumalai site): 72–90° dips, towards E or W, within the Mid-Pliocene Yunshuichi formation (thin-bedded siltstone, mudstone, and sandstone). Grey arrows point bedding. Red arrows point a W-dipping backthrust

15 ka, with alternating phases of limited river aggradation and limited incision. Immediately west of samples 12 and 13, a major fault zone dipping 43°W brings the Late Pliocene Chutouchi pelitic formation on top of the Late Pleistocene terrace deposits and sandy facies of the Early Pleistocene Yuching shale (Fig. 5a), demonstrating the definition of the Kouhsiaoli fault as an active backthrust.

Kouhsiaoli fault slip rate estimate from the Wantan terrace

At the Wantan site (Fig. 6; location in Figs. 1 and 2), located north of Yuching, we identified a linear topographic scarp separating alluvial geomorphic surfaces standing at different elevations. It is oriented N32°E, hence parallel to the Kouhsiaoli Fault, yet also roughly parallel to the Tsengwen River. This configuration questions the formation mechanism of the scarp, by either faulting (fault scarp) or river lateral erosion (terrace riser). Hereafter, we present field observations that advocate for the fault scarp hypothesis and we use the scarp height to estimate a fault slip rate.

In addition to its straightness and its azimuth parallel to the fault, the scarp separates bedrock with distinct lithology and attitudes (Fig. 6a): on the west side, steeply dipping (62–86°ESE) thin beds of siltstone and mudstone, characteristic of the fault hanging wall geology, and on the east side gently dipping (N33°E/24°E) sandstone strata, characteristic of the fault footwall (CPC, 1989; Ho et al. 2005; Fig. 5a). Along a stream, aligned with the scarp (yellow star in Fig. 6a), an outcrop of fair exposure quality (already reported by Liu et al. (2020)) exhibits a steep west-dipping contact of sandstone and muddy sandstone (strata oriented N33°E/80°E) against conglomerate. Some platy pebbles and cobbles have their elongated axis parallel to the contact and gently west-dipping shear zones seem to have propagated within the conglomerate. Since the conglomerate most likely corresponds to remobilized terrace deposits rather than in situ Tsengwen River terrace deposits, the overthrusted conglomerate indicates fault activity possibly as recently as 0.1–1 ka ago. To summarize, the straightness of the topographic scarp, its azimuth, and its location that matches the geological signature of the Kouhsiaoli Fault, lead us to conclude that it is a fault scarp.

Observations of bedrock strath capped by terrace deposits confirm the fluvial origin of the geomorphic surfaces. On both sides of the fault the terrace deposits consist of conglomerate composed of well-rounded pebbles and cobbles (up to 30 cm in diameter), with laminated coarse-to-medium sand lenses and sand layers, capped by clayey fine sand or silt. Compiling strath elevations and topographic profiles along and across the scarp (Fig. 6b, c), we evaluate the thickness of terrace deposits to 6.5–8 m on the hanging wall and to 12 m on the footwall.

Next, we use the scarp height to estimate a fault slip rate. In the lack of ages, we rely on the straightness of the scarp and on the presence of overbank facies on both sides to argue that the scarp mainly formed after the lower terrace was abandoned and that the hanging wall and footwall terraces are parts of the same unit. However, strath observations indicate that terrace deposits are thicker in the footwall (12 m) than in the hanging wall (6.5–8 m) (Fig. 6b, c). Hence, we develop two scenarios for the initial configuration of the terrace top and bedrock strath and development of the scarp (Figure S6, Text S3) and conclude that the true vertical offset is likely comprised between the scarp height measurement (39 ± 5 m) and the difference in strath elevation across the scarp (41 ± 2 m) (Fig. 6b, c). The interval covered by these two ranges is 39 ± 5 m. Next, we examine the footwall terrace height above the modern river for correlation. Heights of 50 m for the top and 37 m for the strath compare with the heights of terrace T1a at Liuchenwan. Therefore, we use an age of 8.6–9.0 ka B.P. for the Wantan terrace. Eventually, the differential uplift rate across the fault is 4.5 ± 0.7 mm/yr. The cumulative slip is calculated from the vertical offset divided by the sine of the fault dip, taken as the same as at Liuchenwan (Fig. 5a), 43° ± 3°. We obtain 57.9 ± 10.6 m, which leads to a fault slip rate of 6.6 ± 1.4 mm/yr.

Holocene uplift rates

Assumptions made in the calculation of bedrock incision include constant river sinuosity and river gradient during the Holocene (Sect. "Rates relative to the coastal plain"). The modern river sinuosity from Hemu to Guji is 2.3 (Fig. 2). Tentative restorations of the paleo-river path were performed by connecting terrace patches of similar age (as in Shyu et al. (2006) for example). Terrace levels T3 and T1a allow for reasonably well-constrained restorations that lead to similar sinuosities of 2.0–2.5. The assumption of a constant river gradient cannot be assessed based on the remaining terraces from Hemu to Guji due to the variable tectonic uplift across the area. Alternatively, we rely on the terraces deposited upstream Hemu (Fig. 2, inset map; Figure S7). These terraces have gradients that are parallel to the modern river, so that our assumption for the downstream reach may be valid as well.

From west to east, the uplift rates relative to the Coastal Plain are 7–11 mm/yr at Guji and Toushe (Table 2; Figs. 2 and 7a). At Guji, the relative uplift rates are very consistent with uplift rates derived from paleosea-level (Table S2; Fig. 7a), which shows that relative uplift rates are representative of tectonic uplift. Eastwards, relative uplift rates strongly increase to reach values between 19 and 24 mm/yr from Luzhihkeng-gou to Cuowei.

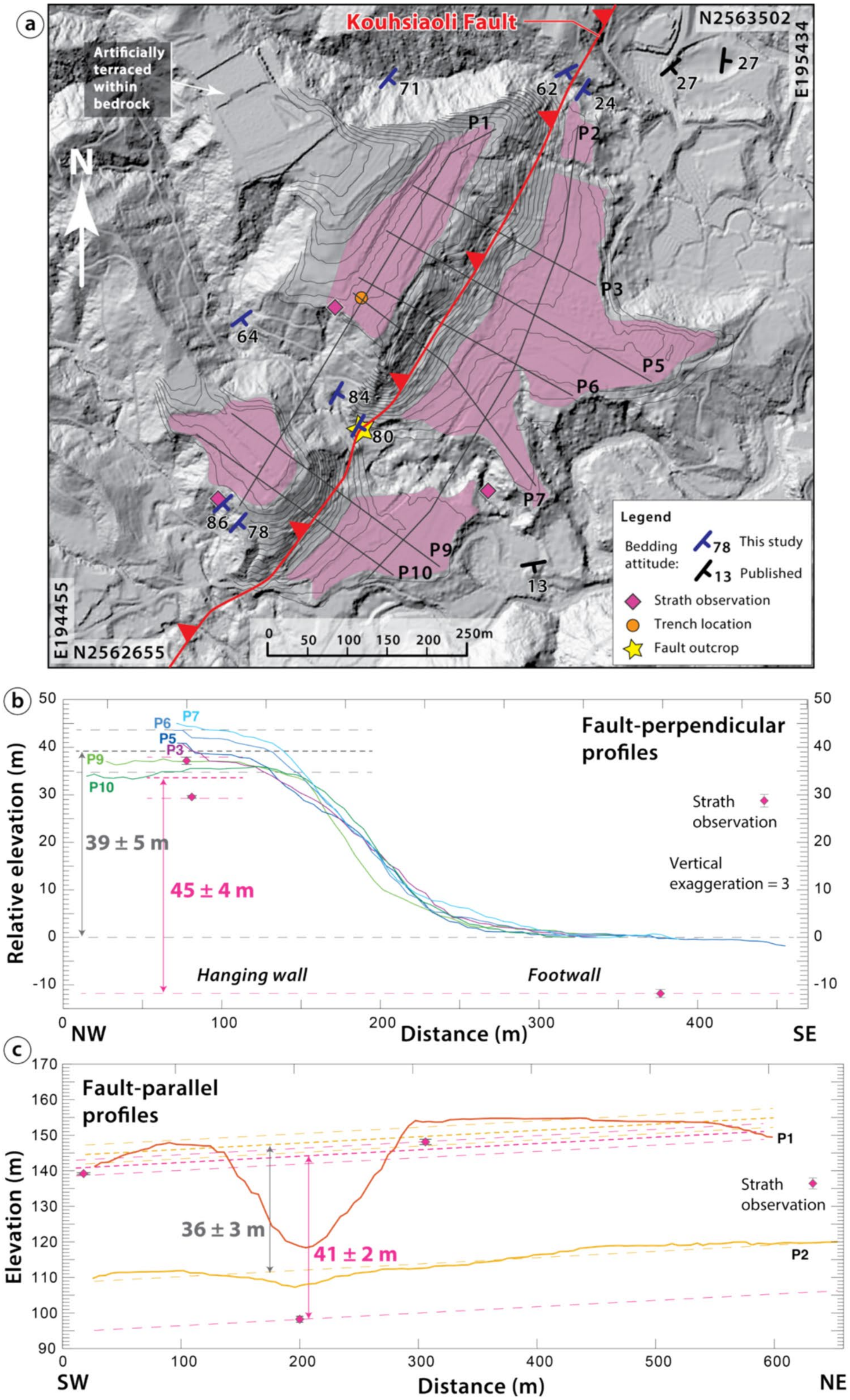

Fig. 6 River terraces across the Kouhsiaoli fault at the Wantan site (see location in Fig. 2). **a** Structural and geomorphic map of the site, over shaded 1-m LiDAR topography (Huang et al. 2020). Topographic contour lines from a 5-m DEM have a 2-m interval. **b**–**c** Vertical offset estimated based on terrace top surface (grey) and terrace strath (magenta) along fault-perpendicular and fault-parallel topographic profiles, extracted from a 5-m DEM. Strath elevations were surveyed by RTK GPS or using measuring tape from terrace top

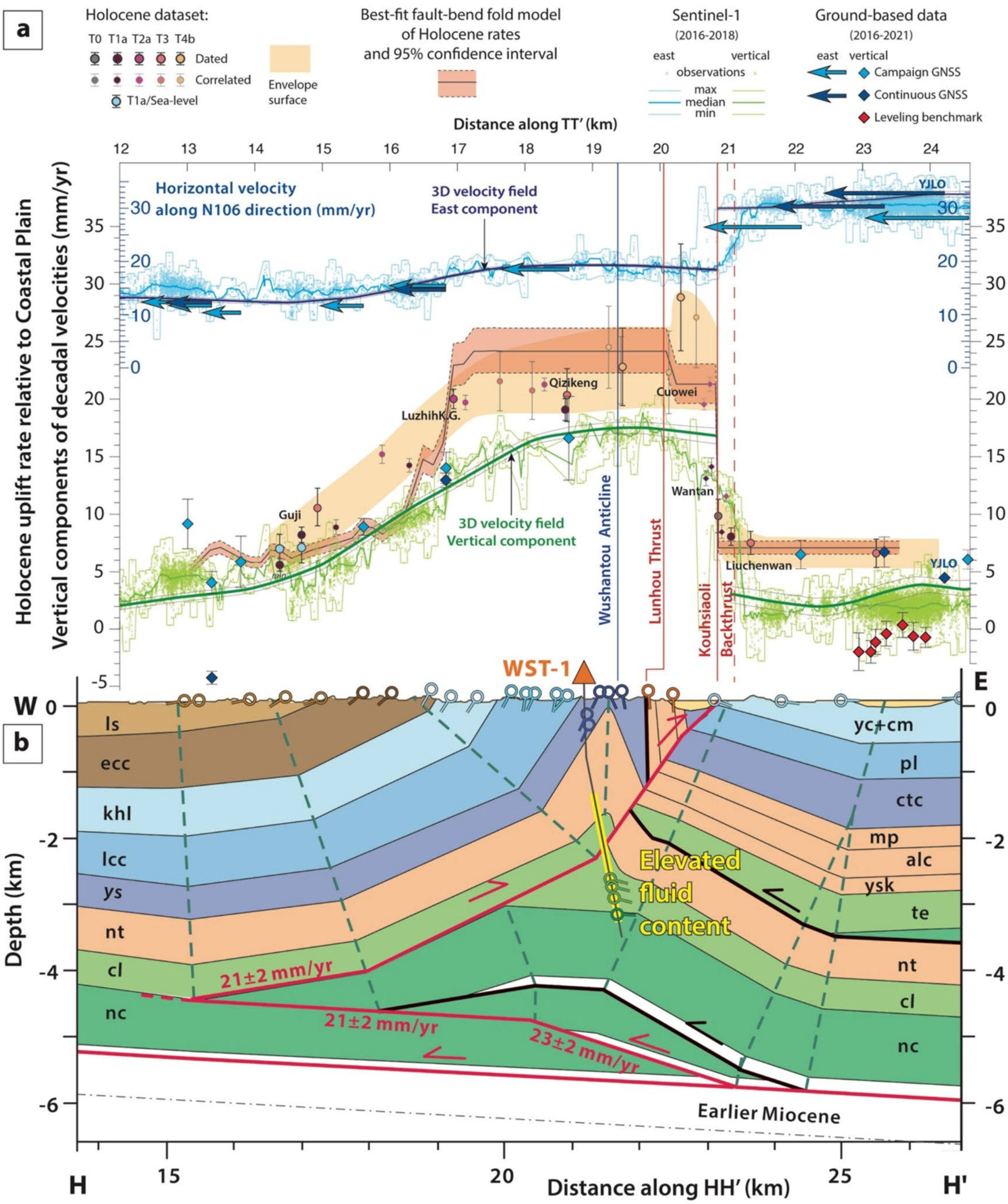

Fig. 7 **a** Geodetic deformation rates and Holocene uplift rates along transect TT', projected onto the cross-section HH' (location in Fig. 1). Distances are anchored at the Kouhsiaoli fault trace (red line), as shown on geological maps along HH' and as observed at the Liuchenwan site (Fig. 5a) projected on TT'. The dashed red line illustrates the location of the inferred fault trace along TT'. All geodetic velocities, as well as inverted velocities, are relative to GNSS station S01R in Taiwan Strait (yellow star in inset map, Fig. 1). GNSS and leveling velocities are from Ching et al. (2021) (Data Set 2). InSAR Sentinel-1 east and vertical components were extracted along a 4-km-wide swath and are from our decomposition of Lu (2022) LOS datasets. The inverted velocity field (east and vertical components shown) is derived from the entire geodetic datasets (Sect. "Geodetic datasets and velocity field inversion"; Fig. 9). **b** Proposed structural model, with active or presumably active structures in red and presumably inactive structures in black. Elevated water content depth range in WST-1 borehole (highlighted in yellow) is from Hsieh and Liu (1971) and Yuan et al. (1987) (Figure S9)

However, at Cuowei, the eastern sites yielded faster rates of 27–29 mm/yr. East of the Kouhsiaoli Fault, relative uplift rates reach lower values of 7–10 mm/yr, as anticipated from outcrops demonstrating the backthrust activity. At Wantan, terrace correlation with terrace level T1a leads to uplift rates of 13–14 mm/yr in the hanging wall, significantly lower than in the Tsoumalai–Cuowei area, and 8–9 mm/yr on the footwall.

Present ground surface deformation

The InSAR LOS datasets offer the best coverage along the investigated structures. The descending orbits (view angle towards west) are optimal to observe deformation across the Kouhsiaoli Backthrust. At the latitude of Yuching, descending LOS velocities from Sentinel-1 show an extremely strong gradient across the inferred fault trace, of about 10 mm/yr across about 200 m, within a broader gradient of about 20 mm/yr across about 1 km (Fig. 8, south transect). This observation supports the idea of a fault creeping at shallow depth and motivated the introduction of a discontinuity in the velocity inversion scheme (Sect. "Geodetic datasets and velocity field inversion"). The resulting 3D velocity field indeed requires this discontinuity to explain the observations, in particular for the east and vertical components (Figs. 7a and 9, S5).

Vertical velocities derived from ascending and descending Sentinel-1 orbits (Figs. 7a and 8) show a progressive increase from 1 to 5 mm/yr in the plain area to 11–16 mm/yr at Luzhihkeng-gou. Further east, uplift rates continue to increase slightly until 15–19 mm/yr at about the Lunhou Fault trace, and then they rapidly decrease towards Liuchenwan, east of which they reach 0–5 mm/yr. GNSS horizontal velocities progressively decrease from east to west, from 29–33 mm/yr east of the Kouhsiaoli Fault to 19 mm/yr near Qizikeng, and 11–14 mm/yr just west of Guji (Figs. 1 and 7a). Overall, 15 to 22 mm/yr of shortening is absorbed across the study area and converted in crustal thickening, with uplift rates up to 19 mm/yr faster near the Wushantou Anticline axis compared to Yuching area. InSAR datasets effectively complement GNSS data. Whereas horizontal GNSS velocities alone do not capture any strong gradient in shortening, the east component derived from Sentinel-1 datasets shows a clear gradient in the order of 12 mm/yr across the Kouhsiaoli Fault. Across the discontinuity allowed at the Kouhsiaoli Fault trace, the 3D inverted velocity field indicates, along TT', shortening of 11 ± 1 mm/yr and a differential uplift of 14 ± 2 mm/yr (Figs. 7a and 9).

The InSAR datasets and our 3D velocity inversion (Figs. 7a, 8 and 9, S3, S4, S5) allow observing along-strike

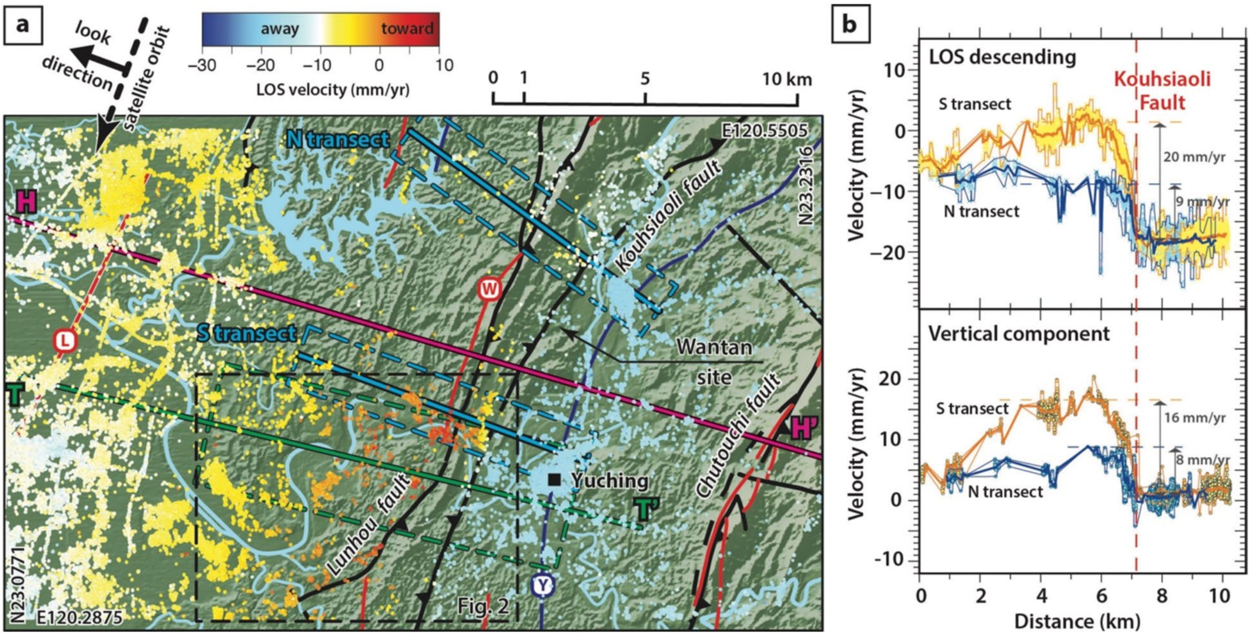

Fig. 8 **a** InSAR line-of-sight (LOS) velocity on Sentinel-1 descending orbit (Lu 2022), relative to S01R (Fig. 1), and observed at individual persistent scatterers. **b** LOS descending velocity and vertical component derived from ascending and descending LOS velocities (Lu 2022) along the N and S transects (2-km-wide swaths). Velocities are relative to S01R and include observations from individual persistent scatterers (yellow and light blue crosses or dots). Thick lines represent the median values, while thin lines represent the minimum and maximum values, all calculated along a 100-m-long window along the transects. LOS velocities include both vertical and horizontal components of displacements, projected along the line-of-sight, which explains the difference with vertical velocities

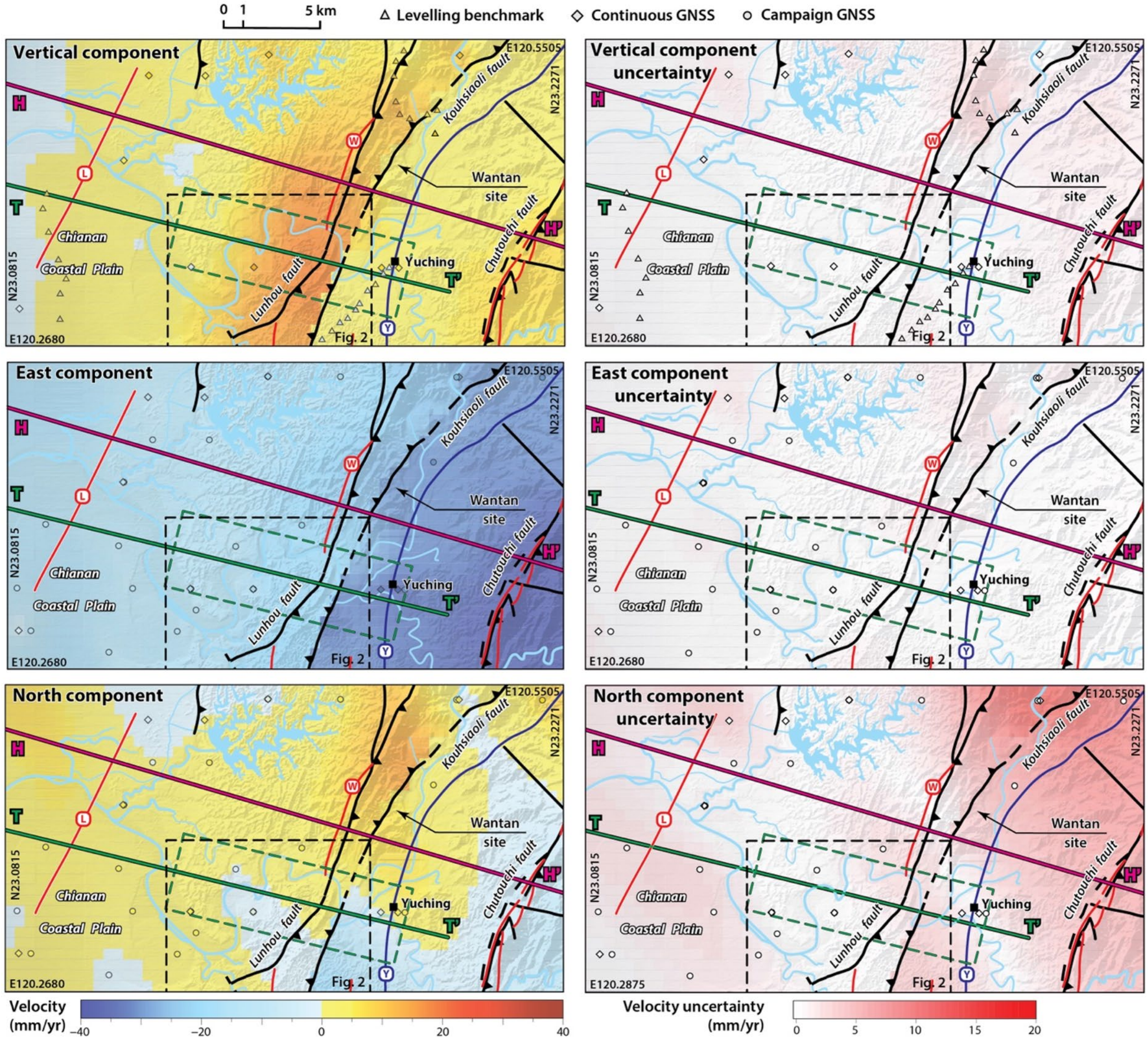

Fig. 9 The three components of the inverted velocity field for the period 2007–2021 and their associated uncertainty, based on ALOS-1 ascending LOS velocities during 2007–2011 (Pathier et al. 2014), Sentinel-1 ascending and descending LOS velocities during 2016–2018 (Lu 2022), and ground-based geodetic measurements during 2016–2021 (Ching et al. 2021). Velocities are relative to GNSS station S01R (Fig. 1)

variations in the deformation rates. Figure 8a clearly shows that LOS velocity gradient across the Kouhsiaoli Fault and uplift along the Wushantou Anticline are larger along TT' and decrease northward. This is also reflected in the vertical component of the inverted velocity field (Fig. 9). Differences in LOS and in vertical velocities are about twice smaller along transect N than along transect S (Figs. 8b and 9). The northward decrease appears to continue until data coverage is lost.

During the inversion process, distinct velocity fields obtained for the ALOS-1 observation period (2007–2021) and for the Sentinel-1 observation period (2016–2021) were found to be comparable (Figure S5), indicating steady deformation rates during the period 2007–2021.

Possible geological structure responsible for the observed surface deformation

Proposed deep geological structure

Constructing a geological cross-section helps determine the possible structural relationship at depth between the individual geological structures observed at the surface. In terms of active deformation, the main players appear to be the Kouhsiaoli Fault and Wushantou Anticline, while the geologically most significant Lunhou Thrust seems inactive. Although we focus on these structures, we need to consider key elements of the geological structure on the west and east, such as the stratigraphic level and depth of the detachments. Nevertheless, other elements, such as the fault-related fold model of the Longtian Anticline at the deformation front, are beyond the scope of this manuscript. While still preliminary for some elements, the cross-section proposed in Fig. 1 still brings a significant advancement with the integration of the Kouhsiaoli Fault as a backthrust, while earlier models drew it as an east-dipping normal fault (Huang 1984; Huang et al. 2004), an overturned thrust (Hickman et al. 2002), or did not include it (Biete et al. 2018).

Beneath the Longtian Anticline, a dense network of seismic lines and deep boreholes image a low-relief west-dipping monocline in the upper 3 km and suggest that the Mid-Miocene Nanchuang Formation (mainly sandstone) lies at 3.5–4.0 km depth and is slightly deformed (Hu and Sheen 1989). Hence, the anticline would grow above a detachment deeper than the top of Nanchuang. At this stage, we draw this fold as a detachment fold. The detachment depth and the limited total shortening are the key pieces of information needed for the present study.

Within the Wushantou Anticline, the WST-1 well documented larger thicknesses than elsewhere for the pelitic Early Pliocene Niaotsui Formation and Late Miocene Chunglun Formation (mainly shale and muddy sandstone), with Nanchuang Formation at 3.5–3.7 km depth (Hsieh and Liu 1971; Yuan et al. 1987) (Figs. 1 and 7b). We propose a triangle zone structure (von Hagke and Malz 2018) that includes a 4- to 5-km-deep wedge of Nanchuang and older Miocene formations and a bedding-parallel passive roof thrust that cross-cuts the east limb of the Wushantou Anticline and the Lunhou Fault to connect with the trace of the Kouhsiaoli Fault. Huang et al. (2004) proposed a similar backthrust within the Yunshuichi shale, probably based on a backthrust observed in the field (Fig. 5b), yet we infer that it would be a minor structure compared to the deeper one within Chunglun Formation. The wedge is proposed to result from a duplex structure ramping from a detachment within Late to Mid-Miocene rocks that would continue westward until the Longtian Anticline, which is probably active.

Classical fault-bend folding model of the Holocene uplift rates

We tested a classical fault-bend fold model to explain Holocene uplift rates. This model assumes that layer thickness and length remain constant during folding, so that slip on a detachment is simply transferred on ramps and uplift is equal to slip multiplied by the sine of the ramp dip-angle (Suppe 1983). In this model, kink bands develop as bedding dip angles parallel to the ramp, so that surface bedding attitudes can be used to approximate the ramp dip (e.g., Yue et al. 2005).

We utilize available surface bedding dips as a proxy for ramp dip on the hanging wall of the Kouhsiali Fault. Across the steep limbs of the Wushantou Anticline (Fig. 7b), from kilometer 19–22.5, we use the ramp dip of 55° inferred from the cross-section and from kilometer 22.5–23.2, we use the Kouhsiaoli Fault dip of 43° observed at Liuchenwan. We include the deeper ramp (in red) and upper detachment, with respective dips of 18° and 4°, and account for the decrease in fault slip across the anticline hinge (Suppe 1983). A Chi-square minimization scheme is used to determine the range of slip rates that best fit the observed Holocene uplift rates on the Kouhsiaoli Fault hanging wall and footwall. Respective weights of 2 and 1 are applied on the dated and correlated terraces to reflect the lower confidence on uplift rates obtained from non-dated terraces. Lower Chi-square values are obtained when the eastern Cuowei rates are excluded. Then, we obtain a best-fit slip rate and 95% confidence interval of 23 ± 2 mm/yr for the deeper ramp, implying a slip rate of 21 ± 2 mm/yr for the Kouhsiaoli Fault (Figs. 7, S8).

The model fits the first-order Holocene uplift pattern well. The resulting Holocene slip rate of 21 ± 2 mm/yr on the upper detachment (4° dip) corresponds to a nearly equal amount of shortening, along the direction N106°. This Holocene shortening rate is consistent with the decadal geodetic shortening rate estimated by subtracting the N106 velocities east of Yuching Syncline axis, 33–35 mm/yr, and those at the mountain front, 11–13 mm/yr (near kilometer 13 along TT' in Fig. 7a). In our model, we ignored the deeper detachment, which contribution to uplift across the entire modeled area would be less than 1 mm/yr, considering a dip of 4° and a slip rate of 10 mm/yr suggested by horizontal velocities near the mountain front. Nevertheless, misfit is significant between Guji and Luzhihkeng-gou, at the eastern Cuowei sites, and for the Wantan hanging wall terrace, located further north from all other sites. Possible causes are discussed in Sects. "Possible geological structure and folding mechanisms" and "Along-strike variations of the geological structures".

Discussion

Mode of slip

Figure 7a displays the large similarity in the patterns of Holocene uplift rates and interseismic vertical velocities derived from InSAR ascending and descending LOS velocities (2016–2018) across the investigated geological structures at the latitude of transect TT'. The vertical component of the 3D inverted velocity field also shows similar variations along the transect.

Decadal and Holocene shortening rate estimates across the entire structure are also in good agreement. The consistency between decadal and Holocene deformation rates indicates that little to no elastic strain has been accumulating during the interseismic geodetic observation period, implying that the source of deformation was slipping mostly, if not fully, aseismically.

Available Holocene and geodetic data hamper to confidently state if the fault has been fully creeping until the surface. The inferred fault scarp in Wantan is about 100 m wide (Fig. 6b), at least partly due to slope degradation processes. Geodetic deformation rates (Figs. 7a and 8, S5) exhibit very sharp gradients within about 100–200 m around the fault trace and a broader gradient of about 1 km in width. We interpret this pattern as a fault that has have been at least partly creeping until the near-surface (probably 100–200 m depth), if not until the surface. Crack survey across man-made structures did not lead to further conclusions. We infer that near-surface deformation could happen as a combination of distributed faulting and folding across a 10- to 100-m-wide zone within recent unconsolidated alluvium. The broader gradient could be related to faster creep at depth or to folding.

Possible geological structure and folding mechanisms

Regarding the source of the observed deformation, our structural investigation resulted in a deeper ramp and a wedge structure, indenting westward beneath a passive roof thrust, the Kouhsiaoli Fault (Fig. 7b). A classical fault-bend model successfully explains the overall pattern of Holocene and interseismic uplift rates (Fig. 7a). However, the model fails to fit the observations at a few locations discussed hereafter, starting with Holocene uplift rates at the eastern Cuowei sites. At eastern Cuowei, the strath elevation is 10–13 m higher than at western Cuowei (Table 2). Radiocarbon sample 10 (sample 3 in Hsieh and Knuepfer (2002)) was collected within a gravel layer just above the strath, which advocates for the representativeness of the bedrock incision rate. We suspect that bedrock strath elevations differ because sites were in the center of the paleo-riverbed or away from it. The model uplift transect also slightly underestimates observations between Guji and Luzhihkeng-gou. Because the fault slip rate is quite fast, an underestimation of ramp dip by a few degrees could explain these differences. To explain those misfits, we may also invoke an additional component of folding originated from pure shear of the volume of rocks, leading to layer thickening, in the core of the Wushantou Anticline.

Along-strike variations of the geological structures

We highlighted the northward decrease in interseismic uplift rates on the hanging wall of the Kouhsiaoli Fault (Fig. 8), with differential uplift rates twice smaller along transect S than along transect N located 1.5 km north of Wantan. The gradient in Holocene uplift rate along transect TT', from Cuowei to Liuchenwan, is 13–19 mm/yr (Fig. 7a). On the other hand, the Holocene vertical slip rate calculated from the Wantan fault scarp is only 4.5 ± 0.7 mm/yr, 3–4 times smaller, keeping in mind the assumptions upon the fault slip rate estimate and the limitation of directly comparing sites at different distances from the fault trace. According to geological maps (CPC, 1989; Ho et al. 2005; Fig. 1), the total separation across the fault also decreases northward, with Mid-Pliocene rocks on top of Early Pleistocene rocks along TT', Mid-Pliocene rocks against Late Pliocene strata at Wantan and a fault mapped within the Maopu shale in the north. Meanwhile, bedding dips just east of the Lunhou Fault decrease from subvertical along TT' to about 35° along transect N, and the trace of the Wushantou fold axis ends near the latitude of transect N. Structures near the topographic front also differ, with the Liuchia Fault and Niushan Anticline also ending at about this latitude (Fig. 1). Consequently, it is likely that the triangle zone structure proposed in our study area extends only until the tip of the Wushantou Anticline. Further north, a different deep geometry would lead to a different kinematics and associated ground surface deformation. At the latitude of TT', no evidence for activity was found on the Lunhou Fault. The fault steepness indeed makes it unlikely to slip as a thrust. Activity on the northern Lunhou Fault, called the Chukou Fault, remains debated, with Lin et al. (2012, 2021a) reporting the fault as active, mainly based on ground-based geodetic observations, including hanging wall uplift relative to the footwall, while the fault was excluded in Shyu et al. (2020) seismogenic structures database.

Along-strike variations in the structural development of the fold-thrust belt in the greater southwestern Taiwan area were proposed to be related to the stratigraphic architecture of the collision host (e.g., Brown et al. 2017, 2022), affected by Paleogene and Early Neogene rift basins, mainly oriented NE–SW. Basin filling resulted in variations in facies and thicknesses, including for the Miocene passive margin sediments and the foreland sequence (e.g., Lin et al. 2003, 2021b). At the latitude of our study area in particular, Late Miocene and foreland sediments become thicker and muddier southward, on the hanging wall of a series of SE-dipping normal faults bounding the Tainan Basin (Lin et al. 2021b; NW corner of Fig. 1). Those changes in lithology and thickness also represent rheology contrasts, which were proposed to play a role in the vergence of thrusts and the development of triangle zone structures (e.g., von Hagke and Malz 2018).

Implications for regional seismic hazards

Aseismic slip considerably reduces the seismic hazard posed by a fault. However, aseismic slip appears as a transient behavior in many natural cases, as well as in rotary shear experiments, and some creeping fault segments were witnessed to slip in earthquakes initiated at their edges or on an adjacent fault segment (see Avouac (2015), Chen and Bürgmann (2017), Harris (2017) for a review). Hence, a creeping fault segment should not be excluded from earthquake hazard assessment.

Under the assumption of a fully locked Kouhsiaoli Fault, and considering a fault length of 15–20 km and a down-dip width of 9.5 km, Leonard (2010) earthquake scaling laws anticipate a maximum earthquake magnitude of 5.3–6.3, with average displacement of 20–60 cm. Given a fault slip rate of 15–20 mm/yr, such an earthquake would happen every 10–40 years. This prediction does not match instrumental seismicity, which implies that creeping has been the dominant mode of slip in the past century. Among the 899 events of a complete catalogue of $M_w \geqq 5.5$ events that occurred during 1900–2006 (Chen and Tsai 2008), only one $M_w5.58$ event (10/03/1962; N23.2 ± 0.05/E120.5 ± 0.05/depth = 5 ± 2.5 km) with depth < 10 km could have occurred on the triangle zone structure that we investigate. Based on the Central Weather Administration catalogue (https://gdms.cwa.gov.tw/catalogDownload.php) during 1973–2023, not a single $M_L > 5$ event was recorded in our study area at depth < 10 km, in agreement with a relocated earthquake catalogue for the period 1990–2020 (Fig. 1). Historical seismicity in Taiwan is documented since the middle of the seventeenth century (Ng et al. 2009). While no event is reported in our study area, the catalogue includes a fair number of events that are unclassified or poorly located, so that we cannot confidently rule out any earthquake occurrence on the investigated structure during that period. Based on the studies on the Chihshang Fault in eastern Taiwan (Ching et al. 2007; Avouac 2015), low coupling was primarily derived at depths shallower than 5 km, which corresponds with the observed steady-state creeping along the fault trace. In contrast, the inferred high coupling distribution aligns with the coseismic slip distribution of the $M_w6.8$ 2003 Chengkung earthquake, mainly at 7–20 km depth. In other words, the lack of earthquakes supports the idea of a mainly or fully creeping Kouhsiaoli Fault.

Factors favoring aseismic slip

Likely factors favoring aseismic slip in our study are a clay-rich lithology and a high fluid content. The WST-1 well documented lithologies based on cuttings and occasional cores and acquired in situ physical properties that are proxies for resistivity and clay content (Hsieh and Liu 1971). Lithology varied from shale to muddy sandstone, with shale being dominant from 1.5 to 3.3 km depth, within the Niaotsui (nt) and Chunglun (cl) Formations (Fig. 7b, S9). Higher water content is also reported at this depth range. Yuan et al. (1987) synthesized fluid pressure information at the regional scale, WST-1 included, and indicated strata rich in fluids from the same stratigraphic units in several wells in the foothills and Coastal Plain.

Earthquake triggering is also a factor known to promote aseismic slip (see Avouac (2015), Harris (2017) and literature review presented in the introduction). Two $M_w > 6$ earthquakes struck the region in 2010 ($M_w6.5$ Jiashian; depth 22.6 km; 30 km ESE of Yuching; Lee et al. 2013) and 2016 ($M_w6.5$ Meinong; depth 14.6 km; 23 km SSE of Yuching; Lee et al. 2016). While they triggered transient events (Huang et al. 2016; Fruneau et al. 2017; Lu et al. 2024) or longer-term changes in the time series of some regional GNSS stations (Ching et al. 2021), our study area was not affected by this phenomenon. Also, aseismic slip was already occurring before these earthquakes based on ALOS-1 InSAR observations and associated inverted velocity field (Figs. 7a and 9, S5).

Conclusions

Along the section of the Western Foothills that we examined, active deformation associated with 20 mm/yr of westward shortening is taken up by folding along the Wushantou Anticline and backthrusting on the Kouhsiaoli Fault, while the geologically most significant Lunhou Thrust appears inactive at this latitude. The structural model that we propose makes the Kouhsiaoli Fault a significant roof thrust with a down-dip width of 9.5 km and a rapid slip rate of 21 ± 2 mm/yr. Folding in the hanging wall would occur mainly as classical fault-bend folding, possibly complemented by pure shear within the core of the Wushantou Anticline, where thick clayey and fluid-rich lithologies were reported.

Active deformation appears to have been mainly or fully aseismic during the geodetic observation period (2007–2021), with clay-rich lithology and elevated fluid content the factors favoring this mode of slip. Instrumental seismicity hints at a similar creep behavior during the past century. Aseismic slip and the length of the structure limited to 15–20 km lower the seismic hazard posed by this rapidly slipping structure. However, we cannot rule out that it could break alongside the northern part of the Lunhou-Chukou Fault or a deeper ramp or detachment.

In most cases previously documented in fold-thrust belts and transpressional setting, aseismic deformation consisted in afterslip following a regional earthquake. Our study reports a case of steady interseismic deformation, associated with slip on a wedge and backthrust, in the context of a fold-thrust belt. We also provide insights on the structural and geological background in which this behavior is occurring, thereby expanding the current knowledge of aseismic deformation in such context.

Supplementary Information

The online version contains supplementary material available at https://doi.org/10.1186/s40562-024-00373-3.

Additional file 1.

Additional file 2.

Additional file 3.

Additional file 4.

Acknowledgements
We thank three anonymous reviewers for their constructive comments and manuscript handling by Editor Kenji Satake. We are grateful to students who helped us in the field surveys: Hsiao-Ting Fang, Ngoc-Thao Nguyen, Chung-Wei Chang, Xiao and Da Yu-Cheng Hsu, Elsayed Abdelbaki, Cheng-Jia Jhuang, Hassan Aleem and Kai-Feng Chen. This work benefitted from discussions with Wen-Shan Chen, Chii-Wen Lin, Wen-Rong Chi, and Andrew Lin. Some figures were generated using the GMT toolbox; with thanks for the developers and community forums.

Author contributions

MLB, CCC, WJH, JWS, YCT, YWC, YCL and MLH conducted geological field survey, terrace mapping and initial field data processing. MLB, CCC and JWS performed the formal terrace data analysis and construction of the cross-section. KEC, EP, CHL and BF provided geodetic datasets and contributed in the 3D velocity field inversion, which was conducted by KEC. MLB prepared the manuscript and figures with significant contributions from CCC, WJH, KEC and EP. All authors read and approved the final manuscript.

Funding
We acknowledge financial support from the Geological Survey and Mining Management Agency (former Central Geological Survey), Taiwan Ministry of Economic Affairs (Project number B10933 to W.J.H.; from data collection to preliminary interpretations) and from the National Science and Technology Council (Grant numbers 108-2116-M-008-027-MY3, 110-2116-M-006-003 and 111-2923-M-008-002-MY4 to M.L.B.; from data collection to final interpretations and publication). This research was also partly funded by the Agence Nationale de la Recherche (ANR), grant ANR-21-CE49-0021. A CC BY license is applied to the AAM arising from this submission, in accordance with the grant's open access conditions.

Availability of data and materials

The data related to Holocene terraces are available in the manuscript and supplementary materials. GNSS and leveling data, as well as the ALOS-1 LOS velocities are provided in supplementary data sets. Sentinel-1 dataset is available from Lu (2022).

Declarations

Competing interests

The authors declare no competing interests.

Received: 11 September 2024 Accepted: 19 December 2024

References

Ainscoe EA, Elliott JR, Copley A, Craig TJ, Li T, Parsons BE, Walker RT (2017) Blind Thrusting, Surface Folding, and the Development of Geological Structure in the Mw 6.3 2015 Pishan (China) Earthquake. J Geophys Res Solid Earth 122:9359–9382. https://doi.org/10.1002/2017JB014268

Argus DF, Gordon RG, DeMets C (2011) Geologically current motion of 56 plates relative to the no-net-rotation reference frame. Geochem Geophys Geosystems. https://doi.org/10.1029/2011GC003751

Avouac J-P (2015) From geodetic imaging of seismic and aseismic fault slip to dynamic modeling of the seismic cycle. Annu Rev Earth Planet Sci 43:233–271. https://doi.org/10.1146/annurev-earth-060614-105302

Barnhart WD, Lohman RB (2013a) Phantom earthquakes and triggered aseismic creep: vertical partitioning of strain during earthquake sequences in Iran. Geophys Res Lett 40:819–823. https://doi.org/10.1002/grl.50201

Barnhart WD, Lohman RB, Mellors RJ (2013b) Active accommodation of plate convergence in Southern Iran: earthquake locations, triggered aseismic slip, and regional strain rates. J Geophys Res Solid Earth 118:5699–5711. https://doi.org/10.1002/jgrb.50380

Biete C, Alvarez-Marron J, Brown D, Kuo-Chen H (2018) The structure of Southwest Taiwan: the development of a fold-and-thrust belt on a margins outer shelf and slope. Tectonics 37:1973–1993. https://doi.org/10.1029/2017TC004910

Bonforte A, Guglielmino F, Coltelli M, Ferretti A, Puglisi G (2011) Structural assessment of Mount Etna volcano from Permanent Scatterers analysis. Geochem Geophys Geosystems. https://doi.org/10.1029/2010GC003213

Brown D, Alvarez-Marron J, Biete C, Kuo-Chen H, Camanni G, Ho C-W (2017) How the structural architecture of the Eurasian continental margin affects the structure, seismicity, and topography of the south central Taiwan fold-and-thrust belt. Tectonics 36:1275–1294. https://doi.org/10.1002/2017TC004475

Brown D, Alvarez-Marron J, Camanni G, Biete C, Kuo-Chen H, Wu Y-M (2022) Structure of the south-central Taiwan fold-and-thrust belt: testing the viability of the model. Earth-Sci Rev 231:104094. https://doi.org/10.1016/j.earscirev.2022.104094

Central Geological Survey, 2021. Map of Active Faults in Taiwan.

Chen KH, Bürgmann R (2017) Creeping faults: Good news, bad news? Rev Geophys 55:282–286. https://doi.org/10.1002/2017RG000565

Chen K-P, Tsai Y-B (2008) A Catalog of Taiwan Earthquakes (1900–2006) with Homogenized Mw Magnitudes. Bull Seismol Soc Am 98:483–489. https://doi.org/10.1785/0120070136

Chen W-S, Ridgway KD, Horng C-S, Chen Y-G, Shea K-S, Yeh M-G (2001) Stratigraphic architecture, magnetostratigraphy, and incised-valley systems of the Pliocene-Pleistocene collisional marine foreland basin of Taiwan. GSA Bull 113:1249–1271. https://doi.org/10.1130/0016-7606(2001)113%3c1249:SAMAIV%3e2.0.CO;2

Chen W-S, Sung S-H, Wu L-C, Hsu H-D, Yang H-C (2004) Shoreline changes in the coastal plain of Taiwan since last glacial epoch. Bull Dept Anthropol 62:40–55

Chen W-S, Yang C-Y, Chen S-T, Huang Y-C (2020) New insights into Holocene marine terrace development caused by seismic and aseismic faulting in the Coastal Range, eastern Taiwan. Quat Sci Rev 240:106369. https://doi.org/10.1016/j.quascirev.2020.106369

Ching K-E, Rau R-J, Zeng Y (2007) Coseismic source model of the 2003 Mw 6.8 Chengkung earthquake, Taiwan, determined from GPS measurements. J Geophys Res 112:B06422. https://doi.org/10.1029/2006JB004439

Ching KE, Gourley JR, Lee YH, Hsu SC, Chen KH, Chen CL (2016) Rapid deformation rates due to development of diapiric anticline in southwestern Taiwan from geodetic observations. Tectonophysics 692:241–251. https://doi.org/10.1016/j.tecto.2015.07.020

Ching K-E, Hu J-C, Chen H-Y, Chang W-L, Cheng K-Q, Chuang Y-R, (2018) Investigation of Active Faults-Stage 4: Observations of Surface Deformation, Data Processing and Analysis, and Fault Inversion Modeling (Report of the Central Geological Survey, Ministry of Economic Affairs)

Ching K-E, Chang W-L, Chuang Y-R, Lee Y-R (2021) Surface deformation observations and seismic hazard assessment at the important active faut areas (1/2) (Report of the Central Geological Survey, Ministry of Economic Affairs)

Copley A, Jolivet R (2016) Fault rheology in an aseismic fold-thrust belt (Shahdad, eastern Iran). J Geophys Res Solid Earth 121:412–431. https://doi.org/10.1002/2015JB012431

Copley A, Reynolds K (2014) Imaging topographic growth by long-lived postseismic afterslip at Sefidabeh, east Iran. Tectonics 33:330–345. https://doi.org/10.1002/2013TC003462

De Guidi G, Barberi G, Barreca G, Bruno V, Cultrera F, Grassi S, Imposa S, Mattia M, Monaco C, Scarfì L, Scudero S (2015) Geological, seismological and geodetic evidence of active thrusting and folding south of Mt. Etna (eastern Sicily): revaluation of "seismic efficiency" of the Sicilian Basal Thrust. J Geodyn 90:32–41. https://doi.org/10.1016/j.jog.2015.06.001

Doin MP, Lodge F, Guillaso S, Jolivet R, Lasserre C, Ducret G, Grandin R, Pathier E, Pinel V (2011) Presentation of the small baseline NSBAS processing chain on a case example: the Etna deformation monitoring from 2003 to 2010 using ENVISAT data. In: Proc. of FRINGE 2011 symposium, Frascati, Italy, 19–23 September 2011, ESA Publication SP-697., PDF

Elliott JR, Bergman EA, Copley AC, Ghods AR, Nissen EK, Oveisi B, Tatar M, Walters RJ, Yamini-Fard F (2015) The 2013 Mw 6.2 Khaki-Shonbe (Iran) Earthquake: insights into seismic and aseismic shortening of the Zagros sedimentary cover. Earth Space Sci 2:435–471. https://doi.org/10.1002/2015EA000098

Fielding EJ, Wright TJ, Muller J, Parsons BE, Walker R (2004) Aseismic deformation of a fold-and-thrust belt imaged by synthetic aperture radar interferometry near Shahdad, southeast Iran. Geology 32:577–580. https://doi.org/10.1130/G20452.1

Fruneau B, Pathier E, Doin M, Hu J-C, Tung H, Doin MP, Walpersdorf A, Volat M (2017) Present-day Deformation in Taiwan Mountain Belt as Monitored by InSAR. In: Presented at the ESA Fringe 2017, Helsinki, Finland. Retrieved from http://fringe2017.esa.int/page_session238.php#391p

Chinese Petroleum Corporation, 1989. Geological map of Tainan.

Harris RA (2017) Large earthquakes and creeping faults. Rev Geophys 55:169–198. https://doi.org/10.1002/2016RG000539

Hickman JB, Wiltschko DV, Hung J-H, Fang P, Bock Y (2002) "Structure and evolution of the active fold-and-thrust belt of southwestern Taiwan from Global Positioning System analysis". In: Byrne TB, Liu C-S (eds.) Geology and geophysics of an arc-continent collision, Taiwan. Geological Society of America, https://doi.org/10.1130/0-8137-2358-2.75

Ho H-C, Shea K-S, Kao M-C, Chen H-W (2005) Geological map of Taiwan. Sinhua Sheet 50

Hsieh C-J, Liu K-H (1971) Subsurface Geological Report of the Wushantou-1 Wildcat, Wushantou Structure. Chinese Petroleum Corporation, Tainan

Hsieh M-L, Lai T-H, Wu L-C, Lu W-C, Liu H-T, Liew P-M (2006) Eustatic sea-level change of 11–5 ka in Western Taiwan, constrained by radiocarbon dates of core sediments. Terr Atmospheric Ocean Sci 17:353–370. https://doi.org/10.3319/TAO.2006.17.2.353(TT)

Hsieh M-L, Knuepfer PLK (2002) Synchroneity and morphology of Holocene river terraces in the southern Western Foothills, Taiwan: A guide to interpreting and correlating erosional river terraces across growing anticlines. In: Byrne TB, Liu C-S (Eds.), Geology and Geophysics of an Arc-Continent Collision, Taiwan. Geological Society of America, pp. 0. https://doi.org/10.1130/0-8137-2358-2.55

Hsu Y-J, Yu S-B, Simons M, Kuo L-C, Chen H-Y (2009) Interseismic crustal deformation in the Taiwan plate boundary zone revealed by GPS observations, seismicity, and earthquake focal mechanisms. Arc-Cont Collis 479:4–18. https://doi.org/10.1016/j.tecto.2008.11.016

Hu C-J, Sheen H-C (1989) An Evaluation on the Hydrocarbon Potential of the Niushan and Lungtien Structures in the Tainan Area. Pet Geol Taiwan 25:11–34

Huang L-S (1984) Iodine contents in formation water from wildcats. Southern Taiwan Pet Geol Taiwan 20:215–235

Huang M-H, Hu J-C, Ching K-E, Rau R-J, Hsieh C-S, Pathier E, Fruneau B, Deffontaines B (2009) Active deformation of Tainan tableland of southwestern Taiwan based on geodetic measurements and SAR interferometry. Geodyn Act Tecton East Asia 466:322–334. https://doi.org/10.1016/j.tecto.2007.11.020

Huang M-H, Tung H, Fielding EJ, Huang H-H, Liang C, Huang C, Hu J-C (2016) Multiple fault slip triggered above the 2016 Mw 6.4 MeiNong earthquake in Taiwan. Geophys Res Lett 43:7459–7467. https://doi.org/10.1002/2016GL069351

Huang S-T, Yang K-M, Wu J-C, Ding H-H, Lee C-C, Mei W-W, Hsu H-H (2004) Investigation on Geological Structure and Crustal Deformation of Taiwan Onshore Faults (5/5)-Comprehensive Analysis of Subsurface Structures in the Western Foothills of Taiwan (Report of the Central Geological Survey, Ministry of Economic Affairs No. 93–13), Research on Active Faults and Earthquake Hazard Assessment

Lambeck K, Rouby H, Purcell A, Sun Y, Sambridge M (2014) Sea level and global ice volumes from the Last Glacial Maximum to the Holocene. Proc Natl Acad Sci 111:15296–15303. https://doi.org/10.1073/pnas.1411762111

Lavé J, Avouac JP (2000) Active folding of fluvial terraces across the Siwaliks Hills, Himalayas of central Nepal. J Geophys Res Solid Earth 105:5735–5770. https://doi.org/10.1029/1999JB900292

Le Béon M, Huang M-H, Suppe J, Huang S-T, Pathier E, Huang W-J, Chen C-L, Fruneau B, Baize S, Ching K-E, Hu J-C (2017) Shallow geological structures triggered during the Mw 6.4 Meinong earthquake, southwestern Taiwan. Terr Atmos Ocean Sci. https://doi.org/10.3319/TAO.2017.03.20.02

Le Béon M, Marc O, Suppe J, Huang M-H, Huang S-T, Chen W-S (2019) Structure and deformation history of the rapidly growing Tainan anticline at the deformation front of the Taiwan mountain belt. Tectonics 38:3311–3334. https://doi.org/10.1029/2019TC005510

Lee S-J, Mozziconacci L, Liang W-T, Hsu Y-J, Huang W-G, Huang B-S (2013) Source complexity of the 4 March 2010 Jiashian, Taiwan, Earthquake determined by joint inversion of teleseismic and near field data. J Asian Earth Sci 64:14–26. https://doi.org/10.1016/j.jseaes.2012.11.018

Lee Y-H, Byrne T, Wang W-H, Lo W, Rau R-J, Lu H-Y (2015) Simultaneous mountain building in the Taiwan orogenic belt. Geology 43:451–454. https://doi.org/10.1130/G36373.1

Lee S, Yeh T, Lin Y (2016) Anomalously Large Ground Motion in the 2016 ML 6.6 Meinong, Taiwan, Earthquake: a synergy effect of source rupture and site amplification. Seismol Res Lett 87:1319–1326. https://doi.org/10.1785/0220160082

Leonard M (2010) Earthquake fault scaling: self-consistent relating of rupture length, width, average displacement, and moment release. Bull Seismol Soc Am 100:1971–1988. https://doi.org/10.1785/0120090189

Lin AT, Watts AB, Hesselbo SP (2003) Cenozoic stratigraphy and subsidence history of the South China Sea margin in the Taiwan region. Basin Res 15:453–478. https://doi.org/10.1046/j.1365-2117.2003.00215.x

Lin C-W, Lu S-T, Chen W-S (2012) Active fault map of Taiwan: an explanatory text (2012 Edition). Spec Publ Cent Geol Surv Minist Econ Aff 26:1–30

Lin AT, Yang C-C, Wang M-H, Wu J-C (2021a) Oligocene-Miocene sequence stratigraphy in the northern margin of the South China Sea: an example from Taiwan. J Asian Earth Sci 213:104765. https://doi.org/10.1016/j.jseaes.2021.104765

Lin C-W, Liu Y-C, Chou P-S, Lin Y-H (2021b) Recent development of active fault investigations of Taiwan. Spec Publ Cent Geol Surv Minist Econ Aff 34:1–40

Liu Y-C, Hsu J-W, Lin C-W (2020) A Study on Structural Characteristics of the Kouhsiaoli Fault, Southern Taiwan. Spec Publ Cent Geol Surv Minist Econ Aff 35:29–47

Lu C-H, Chuang RC, Chiang P-C, Yen J-Y, Ching K-E, Chen Y-G (2024) Detecting infrastructure hazard potential change by SAR techniques on postseismic surface deformation: a case study of 2016 Meinong earthquake in southwestern Taiwan. Eng Geol. https://doi.org/10.1016/j.enggeo.2024.107827

Lu C-H (2022) Data underlying the research on 2D postseismic surface deformation after 2016 Meinong earthquake in SW Taiwan https://doi.org/10.4121/19204863.v1

Mackenzie D, Elliott JR, Altunel E, Walker RT, Kurban YC, Schwenninger J-L, Parsons B (2016) Seismotectonics and rupture process of the MW 7.1 2011 Van reverse-faulting earthquake, eastern Turkey, and implications for hazard in regions of distributed shortening. Geophys J Int 206:501–524. https://doi.org/10.1093/gji/ggw158

Minh DH, Hanssen R, Doin MP, Pathier E (2022) Advanced methods in time series InSAR. In: Surface Displacement Measurement from Remote Sensing Images. John Wiley and Sons, Ltd., pp. 125–153. https://doi.org/10.1002/9781119986843.ch5

Ng SM, Angelier J, Chang C-P (2009) Earthquake cycle in Western Taiwan: insights from historical seismicity. Geophys J Int 178:753–774. https://doi.org/10.1111/j.1365-246X.2009.04164.x

Pathier E, Fruneau B, Doin M-P, Liao Y-T (2014) What are the tectonic structures accommodating the present-day tectonic deformation in South-Western Taiwan? In: A new interpretation from ALOS-1 InSAR and GPS interseismic measurements. Presented at the GEEA Geodynamics and Environment in East Asia: 7th France-Taiwan Earth Sciences Symposium, Nov. 2014, Hualien, Taiwan

Reimer PJ, Austin WEN, Bard E, Bayliss A, Blackwell PG, Ramsey CB, Butzin M, Cheng H, Edwards RL, Friedrich M, Grootes PM, Guilderson TP, Hajdas I, Heaton TJ, Hogg AG, Hughen KA, Kromer B, Manning SW, Muscheler R, Palmer JG, Pearson C, van der Plicht J, Reimer RW, Richards DA, Scott EM, Southon JR, Turney CSM, Wacker L, Adolphi F, Büntgen U, Capano M, Fahrni SM, Fogtmann-Schulz A, Friedrich R, Köhler P, Kudsk S, Miyake F, Olsen J, Reinig F, Sakamoto M, Sookdeo A, Talamo S (2020) The IntCal20 Northern Hemisphere Radiocarbon Age Calibration Curve (0–55 cal kBP). Radiocarbon 62:725–757. https://doi.org/10.1017/RDC.2020.41

Shaw JH, Connors CD, Suppe J (2005) AAPG Seismic Atlas: Seismic Interpretation of Contractional Fault-Related Folds, AAPG Studies in Geology. In: AAPG Studies in Geology. Tulsa, Oklahoma, USA

Shyu JBH, Sieh K, Avouac J-P, Chen W-S, Chen Y-G (2006) Millenial slip rate of the Longitudinal Valley fault from river terraces: implications for convergence across the active suture of eastern Taiwan. J Geophys Res 111:B08403. https://doi.org/10.1029/2005JB003971

Shyu JBH, Yin Y-H, Chen C-H, Chuang Y-R, Liu S-C (2020) Updates to the onland seismogenic structure source database by the Taiwan Earthquake Model (TEM) project for seismic hazard analysis of Taiwan. Terr Atmospheric Ocean Sci 31:469–478. https://doi.org/10.3319/TAO.2020.06.08.01

Suppe J (1980) Imbricated Structure of Western Foothills Belt, Southcentral Taiwan. Pet Geol Taiwan 17:1–16

Suppe J (1983) Geometry and kinematics of fault-bend folding. Am J Sci 283:684–721

Suppe J (1984) Kinematics of arc-continent collision, flipping of subduction, and back-arc spreading near Taiwan. Mem Geol Soc China 6:21–33

Thomas MY, Avouac J-P, Champenois J, Lee J-C, Kuo L-C (2014a) Spatiotemporal evolution of seismic and aseismic slip on the Longitudinal Valley Fault. Taiwan J Geophys Res Solid Earth 119:5114–5139. https://doi.org/10.1002/2013JB010603

Thomas MY, Avouac J-P, Gratier J-P, Lee J-C (2014b) Lithological control on the deformation mechanism and the mode of fault slip on the Longitudinal Valley Fault. Taiwan Tectonophysics 632:48–63. https://doi.org/10.1016/j.tecto.2014.05.038

Tsukahara K, Takada Y (2018) Aseismic fold growth in southwestern Taiwan detected by InSAR and GNSS. Earth, Planets and Space 70:52

von Hagke C, Malz A (2018) Triangle zones–Geometry, kinematics, mechanics, and the need for appreciation of uncertainties. Earth-Sci Rev 177:24–42. https://doi.org/10.1016/j.earscirev.2017.11.003

Walters RJ, Parsons B, Wright TJ (2014) Constraining crustal velocity fields with InSAR for Eastern Turkey: limits to the block-like behavior of Eastern Anatolia. J Geophys Res Solid Earth 119:5215–5234. https://doi.org/10.1002/2013JB010909

Wang H, Wright TJ (2012) Satellite geodetic imaging reveals internal deformation of western Tibet. Geophys Res Lett 39:L07303. https://doi.org/10.1029/2012GL051222

Wu Y-M, Chang C-H, Zhao L, Teng T-L, Nakamura M (2008) A Comprehensive Relocation of Earthquakes in Taiwan from 1991 to 2005. Bull Seismol Soc Am 98:1471–1481. https://doi.org/10.1785/0120070166

Wu Y-M, Shyu JBH, Chang C-H, Zhao L, Nakamura M, Hsu S-K (2009) Improved seismic tomography offshore northeastern Taiwan: implications for subduction and collision processes between Taiwan and the southernmost Ryukyu. Geophys J Int 178(2):1042–1054. https://doi.org/10.1111/j.1365-246X.2009.04180.x

Yang K-M, Rau R-J, Chang H-Y, Hsieh C-Y, Ting H-H, Huang S-T, Wu J-C, Tang Y-J (2016) The role of basement-involved normal faults in the recent tectonics of western Taiwan. Geol Mag 153:1166–1191. https://doi.org/10.1017/S0016756816000637

Yuan J, Huang S-T, Chou T-F, Wu J-C, Lu D-L (1987) The origin of the abnormal pressure zones in Southwestern Taiwan. Ann Explor Prod CPC 10:1–27

Yue L-F, Suppe J, Hung J-H (2005) Structural geology of a classic thrust belt earthquake: the 1999 Chi-Chi earthquake Taiwan (Mw=7.6). J Struct Geol 27:2058–2083. https://doi.org/10.1016/j.jsg.2005.05.020

Zhou Y, Walker RT, Hollingsworth J, Talebian M, Song X, Parsons B (2016) Coseismic and postseismic displacements from the 1978 *Mw* 7.3 Tabas-e-Golshan earthquake in eastern Iran. Earth Planet Sci Lett 452:185–196. https://doi.org/10.1016/j.epsl.2016.07.038

Huang, W-J, C-C Chen, M. Le Beon, IJ Yen (2020), Detailed investigation of characteristics of active faults (2/4), Report of the Central Geological Survey (in Chinese with English abstract).

Publisher's Note